Composites Part B 329 (2027) 114254



Contents lists available at ScienceDirect

Composites Part B

journal homepage: www.elsevier.com/locate/compositesb



Isothermal and non-isothermal friction at thermoplastic composite interfaces

Chunyi Gao [a], Bamber Blackman [b], Zerong Ding [a], Nan Li [a,*]

[a] Dyson School of Design Engineering, Imperial College London, London, UK
[b] Department of Mechanical Engineering, Imperial College London, London, UK

ARTICLE INFO

Keywords:
Interfacial friction
Pull-through test
Thermoplastic composites
CF/PA6
Non-isothermal friction
Friction modelling

ABSTRACT

Interfacial friction plays a critical role in thermoplastic composite forming, and the governing mechanisms depend on the interface type and thermo-mechanical conditions. In this study, interfacial friction in a CF/PA6 system was experimentally characterised under isothermal and non-isothermal conditions using a newly developed pull-through rig with independently controlled normal pressure, temperature, slip-rate and fibre orientation. The investigated interfaces included two ply-ply interfaces, namely woven-woven and UD-woven, and two metal-ply interfaces, namely UD-aluminium and UD-steel. Woven-woven contact was examined as a fully molten interface under isothermal conditions, whereas UD-woven, UD-aluminium and UD-steel contacts were examined under non-isothermal conditions to demonstrate the methodology for characterising diverse interface configurations and thermal states. Under isothermal conditions, woven-woven friction exhibited systematic dependencies on pressure, temperature and slip-rate, consistent with viscous lubrication behaviour. Under non-isothermal conditions, the friction response became interface dependent. For the UD-woven interface, friction depended on the individual pre-contact temperatures of the UD and woven plies, as different temperature pairs with the same average temperature produced different friction levels. In contrast, the UD-aluminium and UD-steel interfaces exhibited limited temperature sensitivity within the tested range. Phenomenological friction models were formulated and calibrated for the four interface types. The calibrated models reproduce the measured parameter trends and provide consistent early-stage and dynamic friction descriptions within a common modelling framework. The study establishes an integrated experimental and modelling framework for interfacial friction characterisation under isothermal and non-isothermal conditions, which can be extended to other thermoplastic composite systems and can provide a basis for simulation-oriented friction modelling.

1. Introduction

The rising demand for lightweight transport structures has increased the use of fibre-reinforced thermoplastic composites and related thermoplastic composite systems [1,2]. Forming processes for these systems have gained increasing attention because of their potential for efficient manufacturing of lightweight components [3]. During forming, in-plane deformation is governed by intra-ply tension and shear, whereas out-of-plane deformation depends strongly on interfacial sliding and bending [4–6]. Carbon-fibre-reinforced polyamide 6 (CF/PA6) is a representative automotive-grade thermoplastic composite material system with broad industrial use. Its in-plane deformation behaviour has been studied extensively [7,8], whereas its interfacial behaviour has received far less attention. Interfacial friction, at both ply-ply and metal-ply interfaces, controls material rearrangement, wrinkle formation and crack initiation, and becomes increasingly important in the forming of complex geometries [9]. Accurate characterisation of this behaviour is therefore important for understanding forming mechanics and supporting friction modelling for simulation.

To date, experimental characterisation of interfacial friction behaviour lacks a standardised methodology, and results remain strongly dependent on the selected test configuration [10–14]. Pin-on-disk methods enable long slip distances but introduce radial pressure gradients, frictional heating and local temperature rises that alter the contact conditions [12,13]. Rotational rheometry provides improved thermal control and defined kinematics but suffers from low output torque, a narrow parameter range and tearing of unidirectional (UD) prepregs [14,15]. In addition to these approaches, two friction test methods

* Corresponding author.
E-mail address: n.li09@imperial.ac.uk (N. Li).

https://doi.org/10.1016/j.compositesb.2026.114254
Received 23 April 2026; Received in revised form 15 September 2026; Accepted 28 September 2026
Available online 29 September 2026
1359-8368/© 2026 The Authors. Published by Elsevier Ltd. This is an open access article under the CC BY license (http://creativecommons.org/licenses/by/4.0/).

derived from ASTM D1894 are widely used, namely the pull-out test and the pull-through test. In the pull-out test, a middle ply is drawn out from between two contact plies, causing a decreasing contact area and non-uniform normal pressure during sliding [10,16]. In contrast, the pull-through test uses a longer middle ply so that the contact area remains constant throughout sliding. The measured friction is therefore more stable and repeatable. However, temperature gradients may develop along the exposed regions of the specimen [5,11,16]. A benchmark study by Sachs et al. [17] using Twintex PP material compared results from different laboratories. Although the pull-through configuration was considered a viable option, the study showed that friction measurements remain highly sensitive to systematic errors such as non-uniform pressure distribution, temperature gradients and sample misalignment [16,17]. These findings demonstrate the need for a robust and well-controlled experimental methodology capable of characterising interface-dependent friction across different material combinations and thermal conditions.

In addition to the challenges associated with test methodologies, interfacial friction behaviour is further complicated by the thermal state of the contacting materials. Both isothermal and non-isothermal conditions can arise in thermoplastic composite forming processes, and these different thermal states can lead to different interfacial responses [18]. Under non-isothermal conditions, the two contacting surfaces may be held at different temperatures, leading to rapid heat transfer upon contact and the development of transient temperature gradients across the interface [3,19]. Under these conditions, the polymer matrix may transition between molten and solid states. Matrix viscosity and crystallisation therefore evolve continuously along the thermal path, with each state associated with a distinct friction response [5,20,21]. As a result, different interfaces may exhibit distinct combinations of viscous lubrication, adhesion and solid contact during sliding [22,23]. Although friction data for individual ply-ply or metal-ply interfaces under selected thermal conditions have been reported, systematic friction characterisation across both isothermal and non-isothermal conditions remains limited [16,24]. A methodology applicable to both thermal states is therefore required to characterise friction behaviour consistently across different interfacial conditions.

Apart from thermal conditions, interfacial friction behaviour in thermoplastic composite forming also depends strongly on the interface type. Interfaces can be broadly classified into ply-ply contact between composite plies and metal-ply contact against a metal counterface. Ply-ply friction is governed by yarn interaction and viscous matrix flow within the contact region [17], whereas metal-ply friction is influenced by ply architecture, matrix flow and metal surface roughness [1,25,26], with recent work on woven jute/PLA prepregs further showing effects of fibre treatment and orientation, normal force and slip velocity [27]. Previous studies [17,24] showed that woven and UD plies exhibit distinct friction responses. Woven plies generate yarn locking and tow nesting during sliding, whereas UD plies provide a smoother sliding path with limited mechanical interlocking. Within UD ply-ply contact, recent C/PAEK work linked the peak response to matrix interlayer thickness and viscosity, while describing the steady-state response through wall slip [28]. Work on carbon fibre/polycarbonate systems further reported that metal-ply friction is higher than ply-ply friction under moderate load due to adhesion or interfacial shear [15]. For CF/PA6 systems, available friction data remain limited. Dörr et al. [29,30] investigated isothermal ply-ply friction in UD CF/PA6 using a pull-through rig and reported that higher slip-rate increases friction, whereas higher normal pressure reduces it under melt-state conditions. Orientation effects were also observed, with 0° alignment producing a stiff response with a sharp peak and 90° alignment resulting in lower steady-state friction. Lang [31] examined metal-ply friction at a UD-steel interface of UD CF/PA6 using an isothermal pull-out configuration and found that friction increased with slip-rate and decreased with temperature and normal pressure, with normal pressure showing the strongest influence. More recently, in situ measurements during thermoplastic composite press consolidation showed that tool-part interaction can evolve from sticking through debonding to sliding and can vary spatially across the interface [32]. Although these studies provide valuable insights, the reported results were obtained under different specimen geometries, fixture configurations and thermo-mechanical conditions [8]. In a comparison of the above ply-ply and metal-ply configurations, Dörr [8] observed systematically lower friction coefficients for the metal-ply interface. However, such differences in test conditions reduce the consistency and reliability of the data for modelling across interfaces. More broadly, studies across thermoplastic composite systems typically focus on specific interface types or isolated processing conditions, and comprehensive datasets covering multiple interfaces under combined pressure, temperature and slip-rate conditions remain limited. This gap restricts the development of transferable friction descriptions across different interface types.

In numerical simulations of thermoplastic composite forming, friction is often simplified as a constant coefficient due to limited experimental data or computational constraints [33]. However, interfacial friction behaviour is strongly influenced by normal pressure, temperature and slip-rate, and these dependencies cannot be represented by a single constant value [34]. Accurate material modelling therefore requires models that reflect the underlying physical behaviour. Existing friction formulations include empirical power laws, Coulomb-viscous combinations and Stribeck-type models linking sliding resistance to matrix viscosity [35–37]. Phenomenological multi-stage models have also been proposed to represent yield and hardening behaviour under varying pressure and temperature conditions [24,38,39]. Although these approaches can capture friction trends within specific systems and processing windows, the underlying datasets and calibrated parameters are typically restricted to particular interface configurations. Consequently, friction models capable of describing interface-dependent behaviour under combined thermo-mechanical conditions within a unified framework remain to be developed.

This study establishes an integrated experimental and modelling framework to address the methodological and modelling limitations identified above in interfacial friction characterisation under isothermal and non-isothermal conditions relevant to thermoplastic composite forming. CF/PA6 is adopted as a representative material system to demonstrate the applicability of the proposed framework. The main contributions of this work are summarised as follows.

- The development of a pull-through rig with integrated thermal and pressure control, enabling stable and repeatable interfacial friction measurements.
- The establishment of an experimental methodology applicable to both isothermal and non-isothermal conditions across multiple interface types, including ply-ply and metal-ply interfaces.
- The generation of a systematic friction dataset under combined thermo-mechanical conditions, including pressure, temperature, slip-rate and interface orientation.
- The formulation of a common phenomenological modelling framework capable of describing interface-dependent behaviour consistently within the investigated thermo-mechanical ranges.

The remainder of this paper is organised as follows. Section 2 describes the design of the pull-through rig and the experimental set-up. Section 3 presents the experimental results and discusses the interface-dependent friction mechanisms. Section 4 introduces the phenomenological friction modelling framework. Finally, Section 5 summarises the key findings and outlines the implications for friction characterisation, modelling and simulation in thermoplastic composite forming.

2. Materials and experimental methods

2.1. Materials

UD CF/PA6 and woven CF/PA6 were selected as the test materials. The UD material was Cetex® TC910 supplied by Toray Advanced Composites, while the woven material was Tepex® dynalite 202-C200 (x)/45% supplied by Bond-Laminates. Single-ply prepregs were used to isolate interfacial sliding and reduce internal ply deformation. Material data from the manufacturers are summarised in Table 1. The investigated interfaces included woven ply against woven ply; UD ply against woven ply; UD ply against aluminium, and UD ply against stainless steel. These interfaces are hereafter referred to as woven-woven, UD-woven, UD-aluminium, and UD-steel. AA6082-T6 aluminium was used and artificially aged at 190 °C for 9 h to stabilise its mechanical properties. The surface was subsequently chromic acid etched to remove contaminants and form a controlled oxide layer, ensuring stable and repeatable interfacial contact. Stainless steel with high surface flatness was selected as the metal counterface for the UD-steel tests to minimise geometric effects during friction testing.

A differential scanning calorimetry (DSC) test was performed to characterise the thermal transitions of the PA6 matrix. Measurements were conducted using a TA Discovery DSC 250 with samples of 15 mg. The temperature was increased from 0 °C to 300 °C at 10 K min^{-1} and then reduced to 0 °C at the same rate. The DSC curve shown in Fig. 1 exhibits a melting peak at approximately 221 °C and a crystallisation peak at approximately 189 °C. These temperatures were used to define the thermal states investigated in the subsequent friction experiments.

2.2. A newly developed pull-through friction rig design and the experimental set-up

This section describes the newly developed pull-through rig used to generate stable interfacial friction data under controlled thermo-mechanical conditions. Fig. 2 illustrates the conventional pull-out test (Fig. 2(a)) and pull-through test (Fig. 2(b)) concepts. In pull-out tests, the contact area decreases during sliding, leading to variations in normal pressure and unstable friction responses. The pull-through concept maintains a fixed contact area but can produce temperature gradients along the unheated free end of the specimen, particularly at high slip-rate. These gradients affect the friction response and limit the applicability of the standard pull-through configuration.

To address these limitations, a modified pull-through configuration was developed, as illustrated in Fig. 2(c), featuring a symmetric layout with integrated heating in the sliding region. The symmetric layout ensures balanced load transfer during sliding and maintains uniform normal pressure across the interface. Integrated heating along the pull-through path is designed to reduce spatial temperature non-uniformity during sliding. By minimising pressure and temperature non-uniformity at the design stage, the developed rig enables stable and repeatable interfacial friction measurements under controlled thermo-mechanical conditions.

Table 1
CF/PA6 material properties [40,41].

	Properties	UD	Woven
Reinforcement			
	Fibre	Carbon	Carbon
	Weaving Style	–	Twill 2/2
	Area Weight (Dry Fabric)	–	200 g/m^2
Matrix			
	Polymer	PA6	PA6
Composite			
	Fiber Volume Content	60 vol.%	45 vol.%
	Thickness Per Layer	0.16 mm	0.25 mm
	Density	1450 kg/m^3	1420 kg/m^3

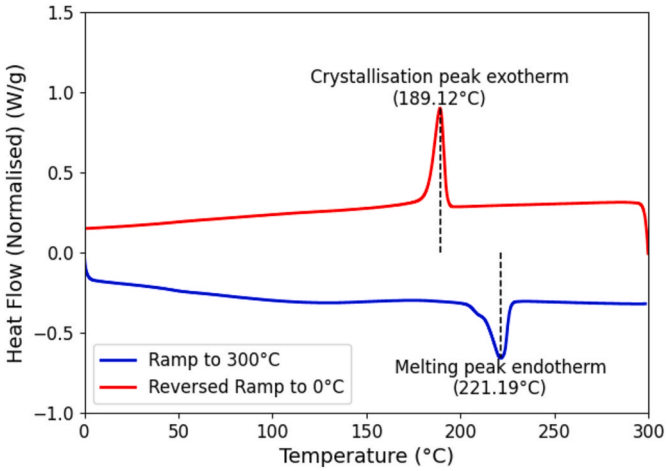


Fig. 1. DSC results for CF/PA6 prepreg.

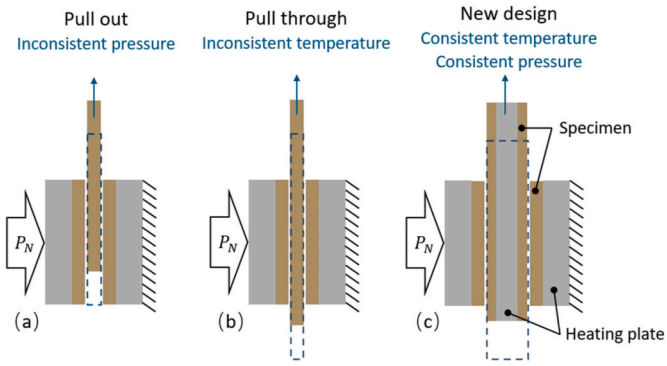


Fig. 2. Schematic comparison of interfacial friction testing methods: (a) pull-out, (b) pull-through, (c) new pull-through. The dashed line marks the initial specimen position, and the shaded area marks the final position.

The detailed design of the testing module is illustrated in Fig. 3(a). The system consists of a heating module and a material mounting module. The heating module incorporates three independently controlled heating plates with embedded cartridge heaters, each regulated by a PID controller, enabling precise control of non-isothermal conditions. This configuration enables the contact surfaces to reach 400 °C from room temperature within approximately 300 s, covering the processing range of most thermoplastic matrices. The heating plates are manufactured from heat-treated H13 steel to ensure thermal stability. Test samples are fixed to mounting plates made from high-conductivity 6-series aluminium alloy. Ceramic insulation sheets limit heat transfer to the surrounding structural components.

The detailed assembly comprising the testing module, pressurising module, and structural support is illustrated in Fig. 3(b). The testing module is incorporated into the assembly to provide controlled thermal conditions during sliding. Controlled normal pressure is applied using a pneumatic SC63 cylinder regulated by a pressure valve and supplied by a portable compressor. The 63 mm bore corresponds to a piston area of 3120 mm^2, producing approximately 1.87 kN at the design limit of 6 bar. For a 60 mm × 60 mm contact area, the corresponding maximum nominal pressure is approximately 0.52 MPa. The cylinder body is manufactured from stainless steel to ensure sealing integrity and durability at elevated temperatures. Stainless-steel structural supports provide overall system rigidity. Three supporting plates connected by pillars mount the heating and pressurising modules, ensuring effective load transfer. A linear guide rail fixed to the machine base constrains the sliding path, maintains in-plane alignment during loading, and allows longitudinal adjustment along the specimen length. Chamfered inlet and

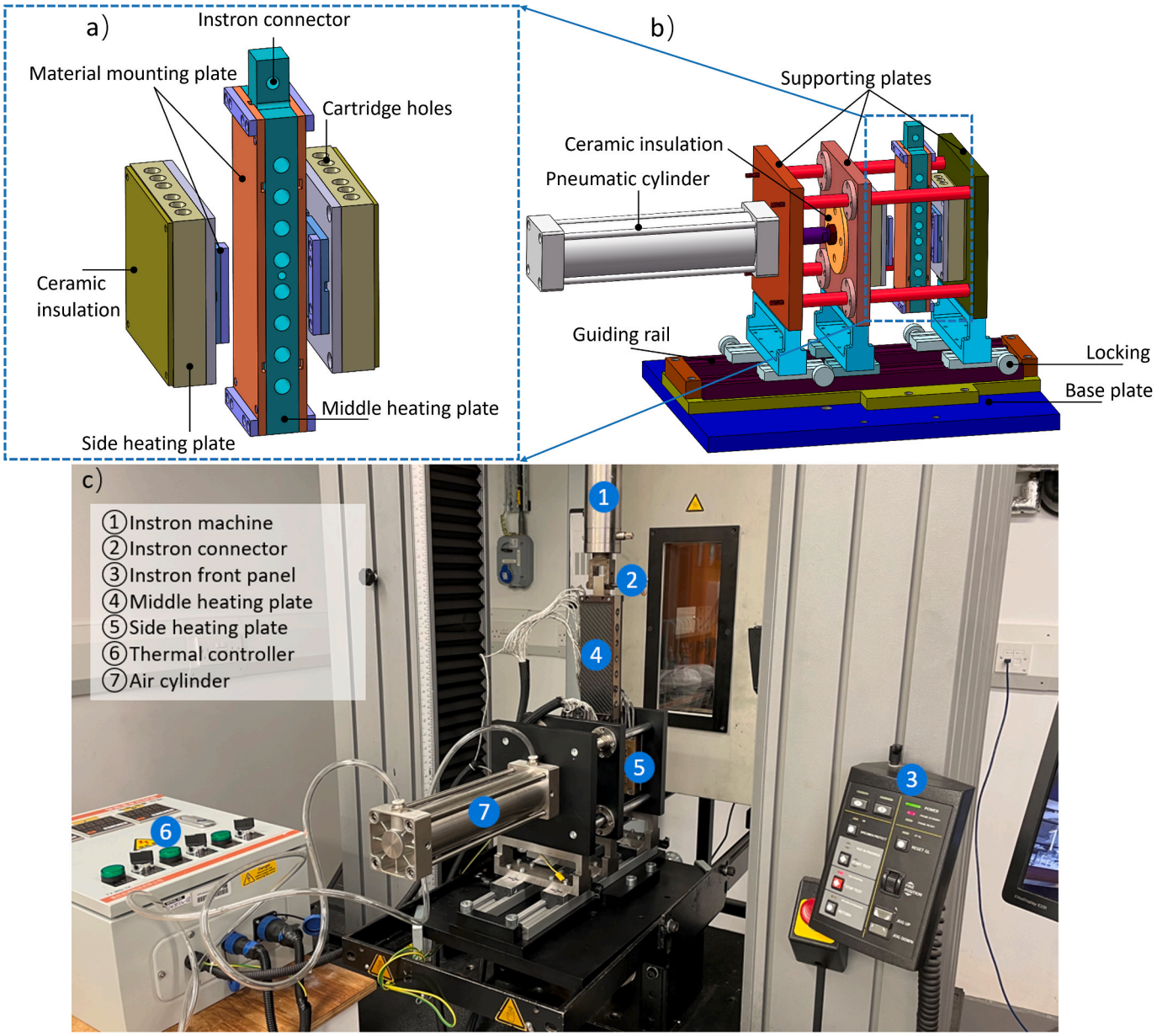


Fig. 3. (a) Testing module comprising the heating and material mounting modules. (b) Detailed assembly comprising the testing module, pressurising module, structural support and guide rail. (c) Laboratory setup with the friction rig mounted on an Instron universal testing machine.

outlet edges minimise interference and local stress concentration, promoting smooth sliding.

The experimental setup is illustrated in Fig. 3(c). The pull-through rig was mounted on an Instron 5584 universal testing machine to provide controlled longitudinal motion at the prescribed slip-rate. Crosshead displacement was transferred through standard adapters to the sliding middle plate (specimen). All contact surfaces were manufactured to match the flatness and surface roughness of industrial forming tools, ensuring their relevance to practical forming conditions.

Temperature was measured using thermocouples attached directly to the mounted material surfaces at the centre, upper-right and lower-left positions of the nominal contact area. Representative pre-contact surface-temperature calibration at target temperatures of 180, 190 and 200 °C showed closely overlapping temperature histories at the three locations and a steady-state spatial variation within ±2 °C (Figure A1 (a)). For these calibration conditions, the thermal controller setpoints were adjusted by approximately +3 °C to compensate for the measured offset; setpoints of 183, 193 and 203 °C produced stable surface temperatures close to 180, 190 and 200 °C, respectively. The same surface-based calibration procedure was used for the other target temperatures. Further calibration details and a representative UD–woven contact-dwell measurement without relative sliding are provided in Appendix A.

2.3. Test conditions

The temperature ranges were selected to examine contrasting thermal configurations relevant to CF/PA6 forming. The UD plies were preheated to 180–200 °C, below the PA6 melting peak, to preserve fibre alignment and restrict squeeze flow [7,42], whereas the woven plies were preheated to 230–250 °C to promote polymer flow and yarn mobility [43]. Aluminium at 320–340 °C and steel at room temperature provided contrasting hot- and cold-metal contact conditions. Normal pressure p, temperature T, slip-rate v and relative orientation φ were controlled independently. For a two-material interface A-B, T_A/T_B denotes the material-surface temperatures immediately before contact,

determined from surface thermocouple measurements as described in Section 2.2. For example, T_u/T_w denotes the UD and woven surface temperatures, respectively. These values specify the initial thermal conditions, while the interface temperature can evolve during sliding. Room temperature is denoted as RT. All test conditions are summarised in Table 2. The specimen set and mounting configurations are shown in Fig. 4.

Post-test surface morphology was documented using a Fujifilm X-S20 digital camera under shadowless illumination, without cleaning before imaging. The woven contact surfaces were examined for woven-woven and UD-woven specimens, and the aluminium counterfaces were examined for UD-aluminium specimens. Millimetre-scale fields of view were selected to capture polymer coverage across multiple woven yarns, downstream accumulation and the spatial distribution of transferred deposits on the aluminium counterfaces. The photographs provide qualitative post-test evidence, rather than direct measurements of interfacial melt-film thickness or continuity during sliding.

2.4. Data processing

Specimen preparation and test configuration followed a consistent procedure to ensure stable interfacial sliding. Before each test, the specimen was placed on the material mounting plates and the two contact surfaces were adjusted to minimise misalignment. After alignment, the materials requiring heating were brought directly from room temperature to their target temperatures and held until the measured surface temperatures stabilised. The normal pressure was then applied pneumatically, followed by crosshead sliding without an intentional contact-dwell period. Load and displacement were recorded continuously using Bluehill software.

For the friction tests, the normal pressure p was applied through the pneumatic loading system. The normal force N acting on a single contact interface was obtained from

$$N = pA \tag{1}$$

where N is the normal force applied to one interface, in N, p is the normal pressure, in kPa, and A is the effective contact area. In this study A was 60 mm × 60 mm.

The friction coefficient μ was calculated from the measured longitudinal force using

$$\mu = \frac{F}{2N} \tag{2}$$

where F is the measured longitudinal force, in N. The factor of two accounts for the two parallel contact interfaces on both sides of the middle heating plate.

To assess the definition sensitivity of the interface-specific early-stage extraction, a common fixed-displacement coefficient, $\mu_{0.5} = \mu\,(0.50\,mm)$, was evaluated for all 42 test conditions. The 0.50 mm location provides a common early-displacement reference before the 4–8 mm dynamic-friction interval, without requiring the interface-specific early-stage features to occur at the same displacement. For each condition, $\mu_{0.5}$ was obtained by linear interpolation of the mean μ-displacement curve and compared with the corresponding primary early-stage value. The absolute percentage difference relative to that value was calculated. These differences were first averaged within each interface and then averaged across the four interfaces with equal weighting. The common coefficient was used only for the definition-sensitivity check, while the primary interface-specific measures were used in the main analysis. The full comparison is provided in Appendix Figure B1.

The Stribeck curve was used to characterise the friction behaviour [44]. The Hersey number He was defined as

$$He = \frac{\eta v}{p} \tag{3}$$

where η is the matrix melt viscosity, in Pa s, v is the imposed slip-rate, in m s^{-1}, and p is the normal pressure. The viscosity-temperature data used to compute η were taken from Ref. [45].

The Stribeck curve was used as a conceptual framework to interpret the friction behaviour. Fig. 5 presents a schematic generalised Stribeck curve adapted from classical tribology [46]. It illustrates three lubrication regimes: boundary lubrication dominated by solid contact; mixed lubrication combining asperity support with a partial melt film; and hydrodynamic lubrication controlled by a continuous polymer film. In the present study, this framework is used to interpret how different interfacial thermal states and contact conditions relate to different friction mechanisms.

3. Results and discussion

This section presents the experimental friction results for the investigated interface types and discusses their underlying mechanisms. For clarity and consistency, the results are organised by interface type. Each interface is analysed with respect to the effects of normal pressure, temperature and slip-rate, with orientation effects discussed where relevant. For each interface, representative μ-displacement curves are first shown to illustrate the characteristic friction response and sliding behaviour. These curves correspond to individual tests and are presented without averaging or numerical smoothing to preserve the intrinsic friction features. For quantitative comparison, an interface-specific early-stage friction measure and the dynamic friction coefficient, μ_k, were extracted from the friction curves and are summarised in the bar charts. For interfaces showing a distinct peak during sliding onset, the static friction coefficient, μ_s, was taken as the first local maximum following the initial high-slope region. For UD–aluminium, where no distinct static-friction peak was observed, the onset descriptor, μ_{on}, characterised the early-stage maximum friction level and was taken as the friction coefficient at the first sampled point beyond 0.50 mm displacement. The dynamic friction coefficient, μ_k, was calculated as the average friction level within a displacement range of 4–8 mm. The distinction between the early-stage and dynamic friction measures is consistent with previous UD C/PAEK ply-ply work, in which peak and steady-state friction were associated with different interfacial mechanisms [28].

Table 2
Summary of test conditions for different interface configurations.

Interface	Normal pressure (kPa)	Temperature (°C)	Slip-rate (mm min^{-1})	Interface orientation/direction pair	Thermal condition
Woven-woven	30, 50, 100	230, 240, 250	20, 200, 500	warp/warp	Isothermal
UD-woven	30, 50, 100	T_u/T_w = 180/230, 185/230,190/240, 195/230,200/250, 180/250,200/230	20, 200, 500	0/warp	Non-isothermal
UD-aluminium	30, 50, 100	T_u/T_{Al} = 180/320, 190/330,200/340	20, 200, 500	0/Al, 90/Al	Non-isothermal
UD-steel	30, 50, 100	T_u/T_{steel} = 180/RT, 190/RT, 200/RT	20, 200, 500	0/steel	Non-isothermal

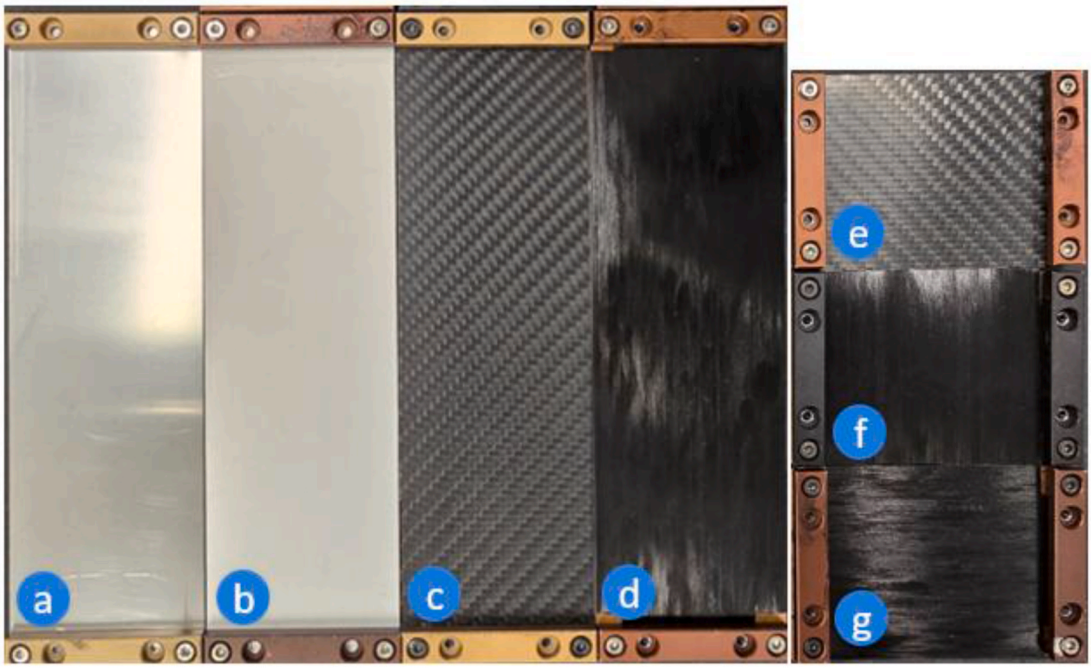


Fig. 4. Specimens and mounting configurations: (a) stainless steel, (b) AA6082, (c) woven CF/PA6, (d) 0° UD CF/PA6, (e) woven CF/PA6, (f) 0° UD CF/PA6, (g) 90° UD CF/PA6. (a-d) mounted on the middle material mounting plate, (e-g) mounted on the side material mounting plate.

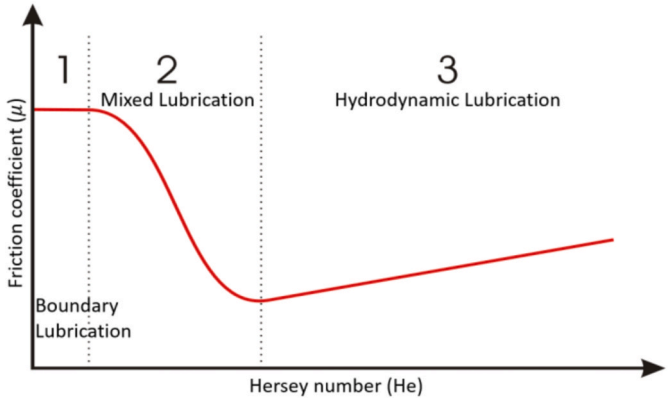


Fig. 5. Schematic generalised Stribeck curve adapted from classical tribology concepts [46].

Each test condition was repeated three times, and the bar charts report the mean values with error bars indicating the standard deviation. Three repeat curves for representative high-friction and peak-prone conditions are superimposed in Appendix Figure C1. All four interface types are included, with an additional high-slip-rate woven–woven condition because this interface exhibited the most pronounced early-stage peak.

The fixed-displacement check gave an interface-balanced mean absolute percentage difference of 9.4% relative to the primary interface-specific early-stage measures (Appendix Figure B1). All 13 parameter groups retained the same direction of change between their first and last conditions, and the complete within-group ranking was preserved in 12 of 13 groups. The only change in ranking occurred in the closely clustered UD–steel temperature series, for which neither extraction method showed a clear monotonic temperature trend. Thus, the extraction definition affected the numerical values of the early-stage coefficients, while the main qualitative parameter trends remained consistent.

3.1. Woven-woven

Woven-woven friction was characterised under isothermal conditions with independently controlled normal pressure, temperature and slip-rate. This configuration provides a reference case for fully molten ply-ply contact.

Under varying normal pressure, shown in Fig. 6(a) and (d), both μ_s and μ_k decrease with increasing pressure. This trend is consistent with pressure-assisted spreading of the molten polymer across the yarns, promoting a more continuous and uniform interfacial melt film. Improved melt coverage can reduce the contribution of local yarn-yarn interaction to sliding resistance. At lower pressures, less uniform melt coverage may allow these interactions to remain relevant even though the plies are already molten. The pressure dependence is therefore interpreted in terms of the formation and uniformity of the interfacial melt film.

The post-test woven contact surfaces in Fig. 7 show more pronounced downstream polymer accumulation at 100 kPa than at 30 kPa, with polymer coverage also visible over the yarns. These features support pressure-assisted polymer spreading and redistribution, consistent with the proposed improvement in interfacial melt-film continuity and uniformity at higher pressure.

The temperature dependence of the woven-woven interface is shown in Fig. 6(b) and (e). Increasing the temperature from 230 °C to 250 °C reduces both μ_s and μ_k. The reduction in friction coefficient at higher temperature is consistent with lower melt viscosity and enhanced polymer flow. Improved polymer spreading can fill inter-yarn gaps and reduce the contribution of local yarn contact, consistent with the lower friction level. These results support a substantial viscous-shear contribution within the melt film.

The slip-rate dependence of the woven-woven interface is shown in Fig. 6(c) and (f). Increasing the slip-rate raises both μ_s and μ_k because the molten polymer has less time to relax during sliding, resulting in higher viscous shear within the interfacial melt film. At lower slip-rates, the molten polymer has sufficient time to redistribute and relax, leading to reduced viscous shear stress and lower friction levels. The response is consistent with a rate-dependent viscous mechanism in which the

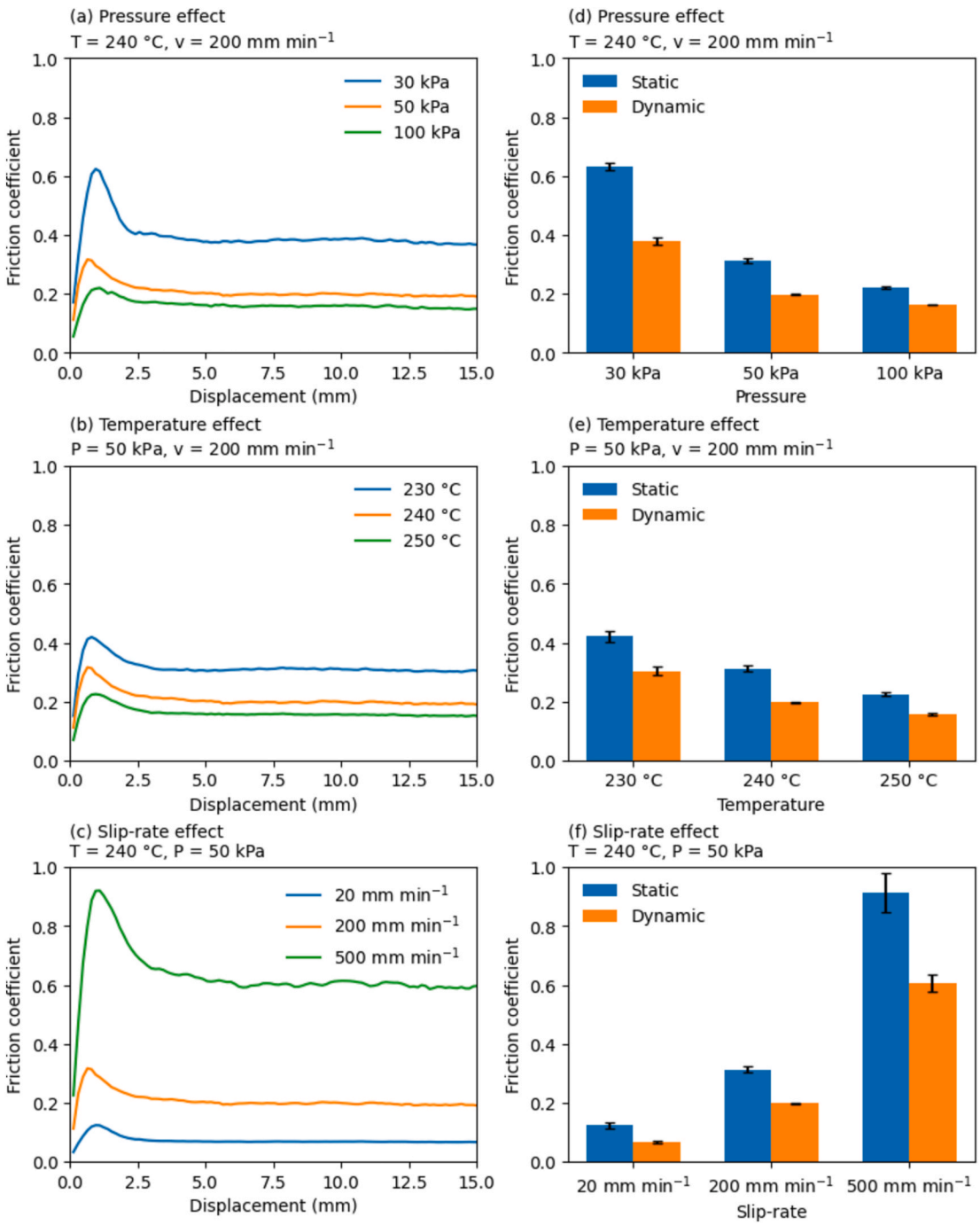


Fig. 6. Influence of normal pressure, temperature and slip-rate on woven-woven friction behaviour. (a-c) μ-displacement curves and (d-f) corresponding static and dynamic friction coefficients.

molten polymer makes a substantial contribution to sliding resistance.

A more pronounced early-stage peak is observed at higher slip-rate. At higher slip-rates, less time is available for polymer spreading and redistribution during early sliding, which may contribute to the higher initial friction response. At low slip-rate, more time is available for polymer spreading and redistribution during early sliding, resulting in a weaker peak. Overall, woven-woven friction is mainly influenced by viscous shear within the melt film and the time available for polymer redistribution during sliding.

The dependence of μ_s and μ_k on the Hersey number *He* is shown in Fig. 8. Both friction measures increase with *He*, consistent with a substantial viscous-shear contribution and with the trend represented by the hydrodynamic branch (Region III) of the Stribeck framework. The monotonic $\mu_s - He$ and $\mu_k - He$ relations bring together the effects of pressure, temperature and slip-rate, supporting a predominantly melt-film-controlled response across the tested conditions. Local yarn-yarn interactions may nevertheless remain relevant where melt coverage is less uniform. Similar hydrodynamic behaviour has been reported for other thermoplastic carbon-fibre systems at elevated temperature [17, 29].

3.2. UD-woven

UD-woven friction was characterised under non-isothermal condi-

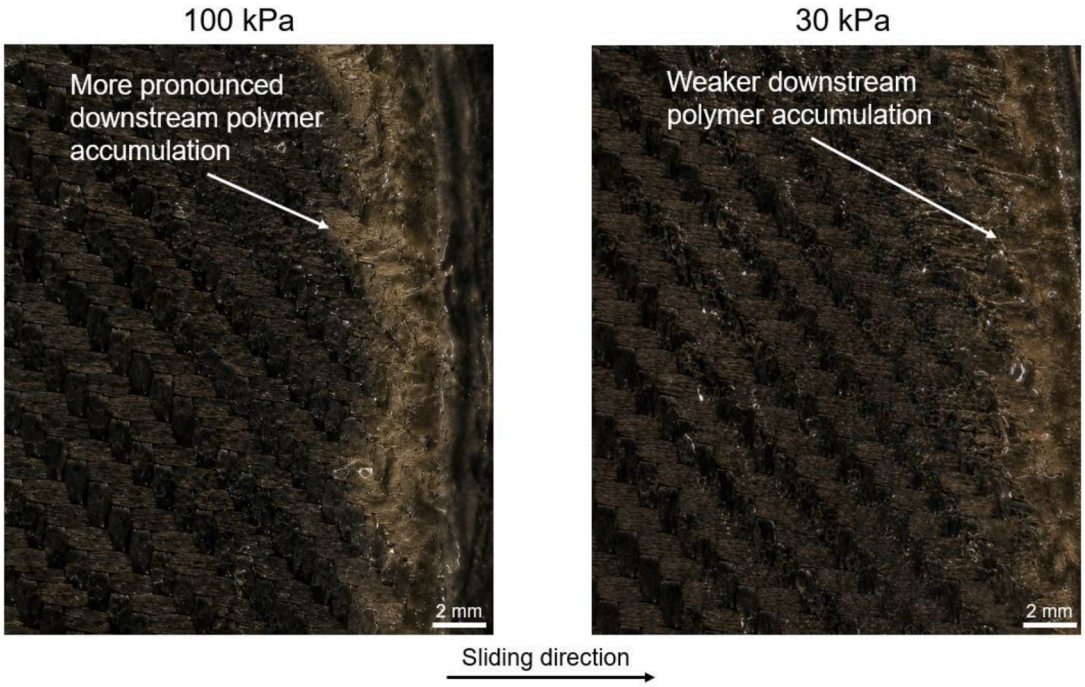


Fig. 7. Post-test woven contact surfaces from woven-woven friction tests at 100 kPa and 30 kPa (left and right, respectively), with $T = 240\,^{\circ}C$ and $v = 200\ mm\ min^{-1}$. The sliding direction is indicated. Scale bars: 2 mm.

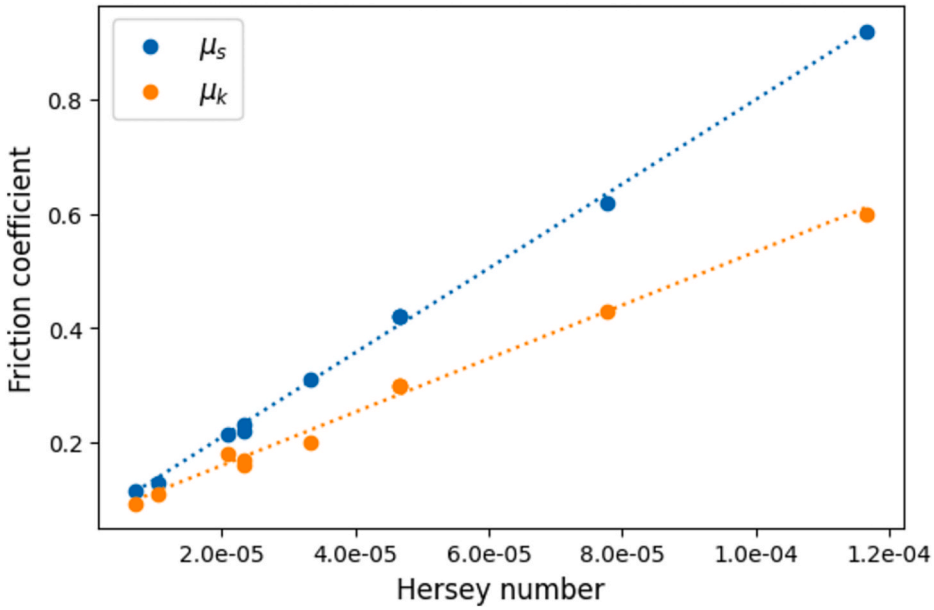


Fig. 8. Experimental Stribeck curve for woven-woven contact under different test conditions.

tions with independently controlled normal pressure, temperature and slip-rate. Before contact, the UD ply was heated to a temperature below the polymer melting point ($T_u < T_m$) to preserve fibre alignment and restrict squeeze flow [7,42], while the woven ply was heated above the melting point ($T_w > T_m$) to promote polymer flow and yarn mobility [43]. This temperature arrangement provides an initially solid-melt ply-ply configuration under non-isothermal conditions.

The pressure dependence of the UD-woven interface is shown in Fig. 9(a) and (d). Increasing the normal pressure reduces both μ_s and μ_k. Higher pressure compresses the molten woven layer against the UD surface and can promote more uniform polymer spreading and greater melt coverage across the interface. This redistribution can fill inter-yarn gaps and reduce the contribution of local solid contact, consistent with the lower friction coefficient. Here, melt coverage refers to the extent to which the molten polymer from the woven ply covers the opposing UD surface. Greater melt coverage can promote a more continuous and uniform interfacial melt film, allowing a larger contribution from viscous shear within the molten layer. More limited melt coverage at low pressure may leave regions with less polymer coverage and greater local solid contact. The pressure dependence is therefore interpreted in terms of melt coverage and the balance between viscous shear and local solid contact.

The temperature dependence of the UD-woven interface is shown in Fig. 9(b) and (e). The friction response reflects the coupled thermal

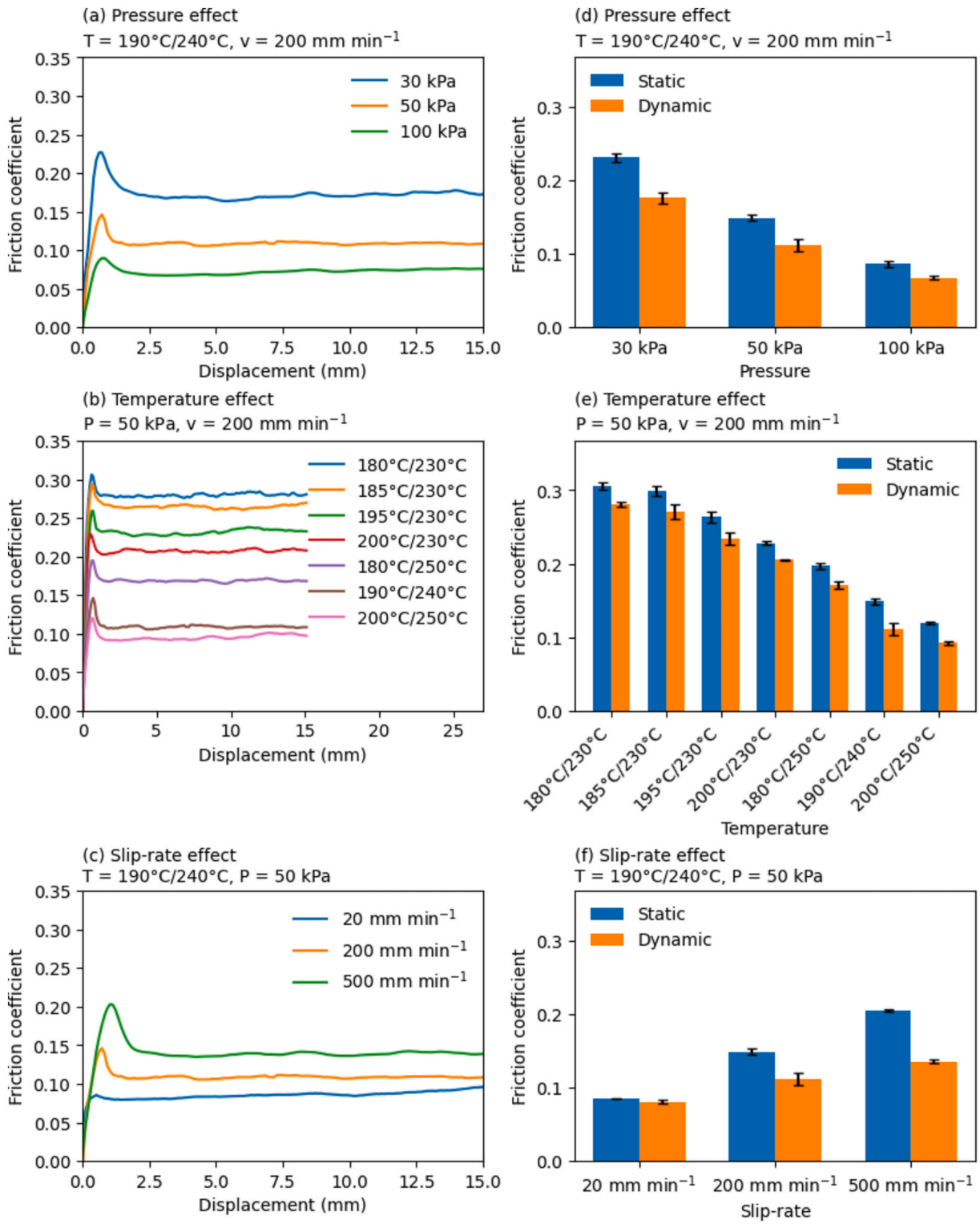


Fig. 9. Influence of normal pressure, temperature and slip-rate on UD-woven friction behaviour. (a-c) μ-displacement curves and (d-f) corresponding static and dynamic friction coefficients.

behaviour of the two materials. For fixed T_u at 180 °C or 200 °C, increasing T_w from 230 °C to 250 °C reduces both μ_s and μ_k. Higher T_w lowers the initial woven-matrix viscosity and increases yarn mobility, favouring polymer flow and melt coverage during contact and sliding. At lower T_w, the higher matrix viscosity may restrict polymer flow, leading to less uniform lubrication and a higher friction coefficient. For fixed T_w at 230 °C, both μ_s and μ_k decrease as T_u increases from 180 °C to 200 °C. Changes are small between 180 and 185 °C, whereas a stronger temperature sensitivity is observed between 195 and 200 °C. These temperature intervals lie on either side of the DSC crystallisation peak of approximately 189 °C, which therefore provides a physically informed reference for the UD-temperature response. The stronger response at higher T_u may reflect changes in surface mobility and wetting during contact.

Fig. 10 compares the post-test woven contact surfaces at $T_u/\ T_w =$ 200/230 °C and $T_u/T_w =$ 200/250 °C. At 200/230 °C, the woven-yarn texture is more clearly visible, whereas at 200/250 °C the polymer coverage is more extensive and downstream accumulation is more pronounced. These observations on the woven side support enhanced polymer redistribution at higher T_w and the melt-coverage interpretation of the lower friction coefficients in Fig. 9(b) and (e).

To assess the coupled temperature influence, three configurations with the same mean pre-contact temperature of 215 °C were compared: 200/230 °C, 180/250 °C, and 190/240 °C. The 200/230 °C configuration gave the highest friction of the three, the 180/250 °C configuration gave intermediate values, and the 190/240 °C configuration gave the lowest friction. At 200/230 °C, the lower woven temperature may restrict initial polymer flow, whereas at 180/250 °C the cooler UD surface may limit wetting and promote faster heat transfer from the molten woven layer. The 190/240 °C combination is consistent with a more favourable balance between polymer flow and UD surface mobility. The distinct friction levels show that the mean pre-contact temperature alone does not describe the response.

To further assess the coupled temperature effect, an additional configuration of 200/250 °C was tested. This configuration produced the lowest friction coefficients among the tested temperature combinations, consistent with a combination of greater initial woven-matrix mobility and more favourable wetting of the warmer UD surface. The difference between the 190/240 °C and 200/250 °C cases was smaller than that between the 190/240 °C and 200/230 °C cases. These results indicate weaker temperature sensitivity towards the higher-temperature end of the tested combinations and are consistent with a melt-coverage contribution to lubrication. The observed changes in temperature sensitivity, together with the DSC crystallisation temperature, provide the basis for the temperature breakpoints adopted in the phenomenological model in Section 4.2.

The slip-rate dependence of the UD-woven interface is shown in Fig. 9(c) and (f). Increasing the slip-rate raises both μ_s and μ_k. At higher slip-rates, faster shearing of the molten woven matrix and less time for polymer redistribution can increase the friction coefficient. At low slip-rates, more time is available for the molten polymer to spread over the UD surface, which may improve melt coverage and reduce friction.

The early-stage peak in the μ-displacement response is also more pronounced at higher slip-rate. At low slip-rate, greater polymer redistribution during early sliding may shorten the initial sticking region and reduce the peak. At high slip-rate, local solid contact may persist while the molten polymer spreads over the UD surface, producing a sharper transition to sliding. This behaviour is consistent with a changing balance between viscous shear in the molten polymer and local solid contact during early sliding.

3.3. UD-aluminium

UD-aluminium friction was characterised under non-isothermal conditions with independently controlled normal pressure, temperature, slip-rate and fibre orientation. In this configuration, the UD ply and the aluminium sheet were heated to different pre-contact temperatures to create a non-isothermal metal-ply contact state. The UD ply temperature T_u was set below the melting point at 180 °C, 190 °C and 200 °C, while the aluminium sheet temperature T_{Al} was set at 320 °C, 330 °C and 340 °C. This configuration provides a representative solid-hot metal interface under non-isothermal conditions.

The pressure dependence of the UD-aluminium interface is shown in Fig. 11(a) and (d). Increasing the normal pressure reduces both μ_{on} and μ_k. Contact between the initially solid UD ply and the hot aluminium surface can soften or melt the interfacial PA6, promoting polymer redistribution between the fibres and the metal.

The post-test aluminium counterfaces in Fig. 12 show more extensive polymer-rich deposits with adhered fibres at 100 kPa, whereas patchier deposits are observed at 30 kPa. This contrast is consistent with pressure-assisted polymer redistribution and, together with the friction results, supports its proposed contribution to interfacial lubrication within the tested pressure range.

The temperature dependence of the UD-aluminium interface is shown in Fig. 11(b) and (e). No clear temperature dependence was observed for either μ_{on} or μ_k within the tested non-isothermal temperature pairs. This limited sensitivity is consistent with the relative contributions of polymer-mediated shear and local fibre-metal contact remaining broadly similar along the tested thermal path.

The slip-rate dependence of the UD-aluminium interface is shown in Fig. 11(c) and (f). Increasing the slip-rate raises both μ_{on} and μ_k. At higher slip-rate, the softened PA6 layer is sheared more rapidly and has less time to relax, so the interfacial shear stress increases and the friction level rises. At lower slip-rate, the softened layer can deform and relax

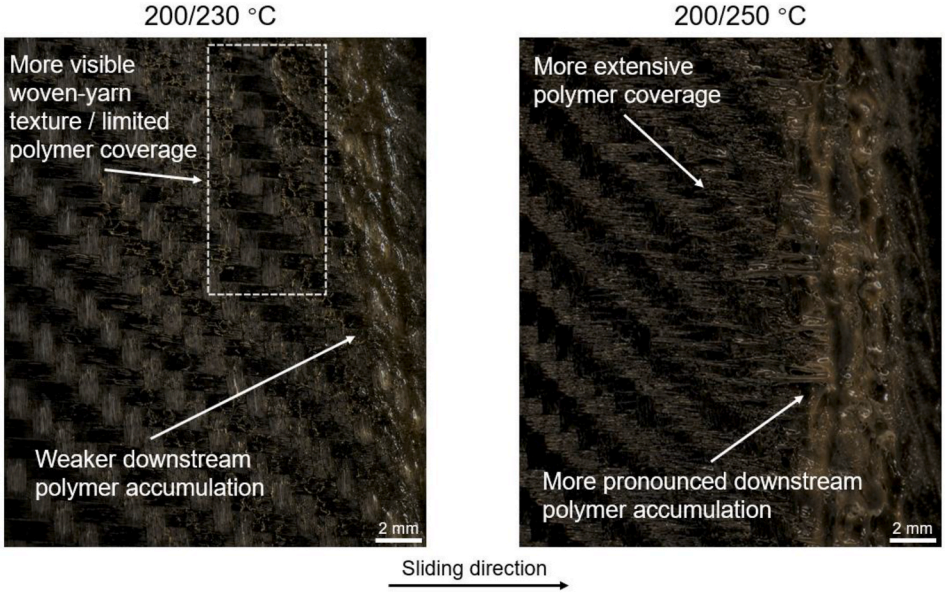


Fig. 10. Post-test woven contact surfaces from UD-woven friction tests at $T_u/T_w =$ 200/230 °C and $T_u/T_w =$ 200/250 °C (left and right, respectively), with $p =$ 50 kPa and $v = 200\ mm\ min^{-1}$. The sliding direction is indicated. Scale bars: 2 mm.

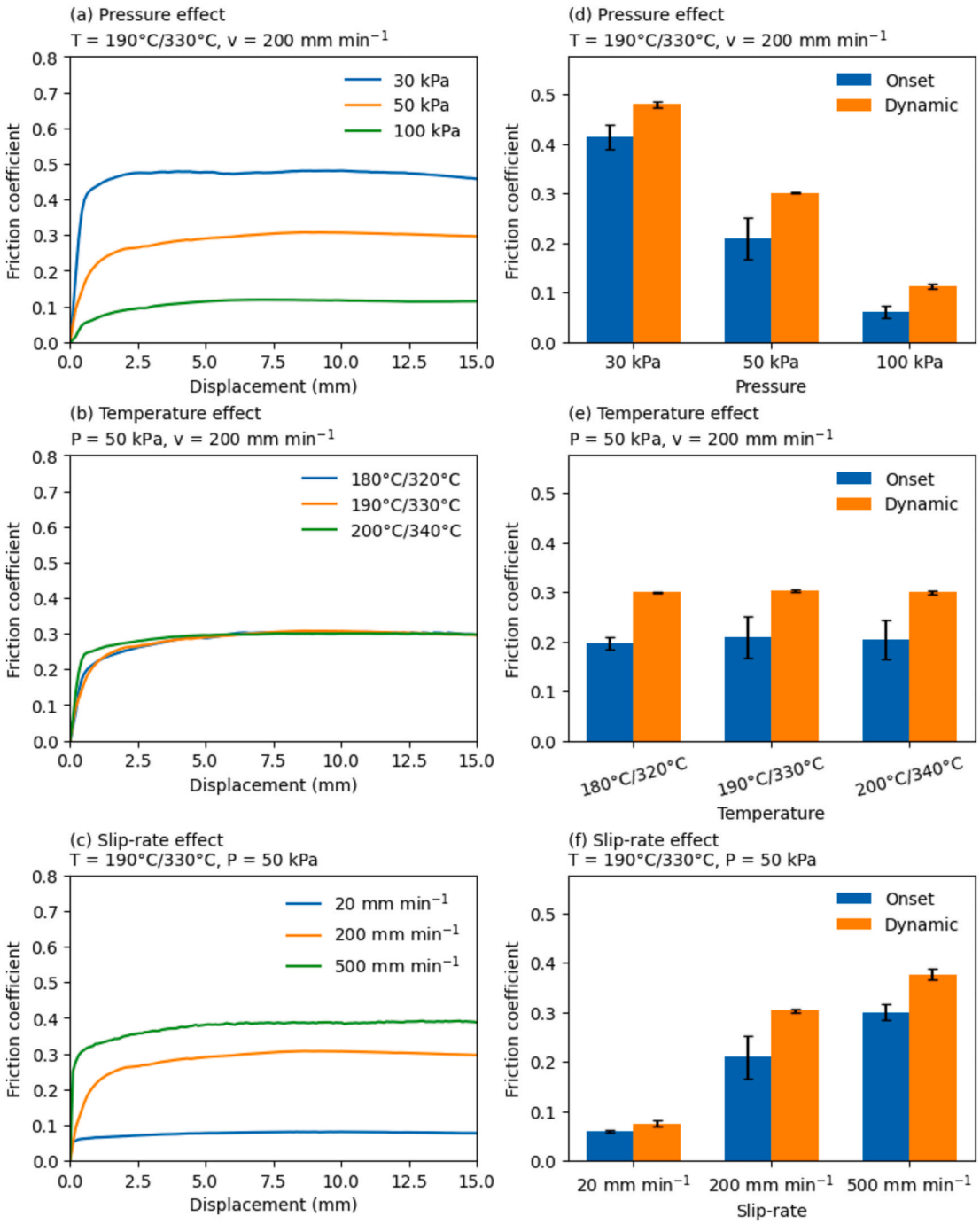


Fig. 11. Influence of normal pressure, temperature and slip-rate on UD-aluminium friction behaviour. (a-c) μ-displacement curves and (d-f) corresponding onset and dynamic friction coefficients.

during sliding, which reduces friction.

The absence of a distinct static-friction peak is evident in the μ-displacement curves. A softened or molten PA6 layer at the interface may accommodate early motion through viscous deformation, leading to a gradual transition to sliding rather than a distinct static-friction peak. The early-stage value defined in Section 3 is therefore reported as an onset descriptor, μ_{on}, for quantitative comparison, while μ_k characterises the later sliding response.

The orientation dependence of the UD-aluminium interface was assessed under identical thermo-mechanical conditions, and the results are shown in Fig. 13. In the early stage, at displacement $u < 2$ mm, both 0°/Al and 90°/Al exhibit a rapid rise in μ, consistent with polymer softening and a substantial polymer-mediated contribution. The initial friction levels are similar before the orientation responses begin to diverge. In the intermediate stage, at $2 \leq u \leq 6$ mm, the increasing difference may reflect a greater contribution from fibre-metal interaction. The 90° configuration develops a higher friction level because the transverse fibres oppose shear more strongly, whereas the 0° fibres, aligned with the sliding direction, are associated with a lower friction level. In the steady stage, at $u > 6$ mm, both curves stabilise, but the 90° orientation retains a higher μ, consistent with greater tangential resistance associated with transverse fibre engagement.

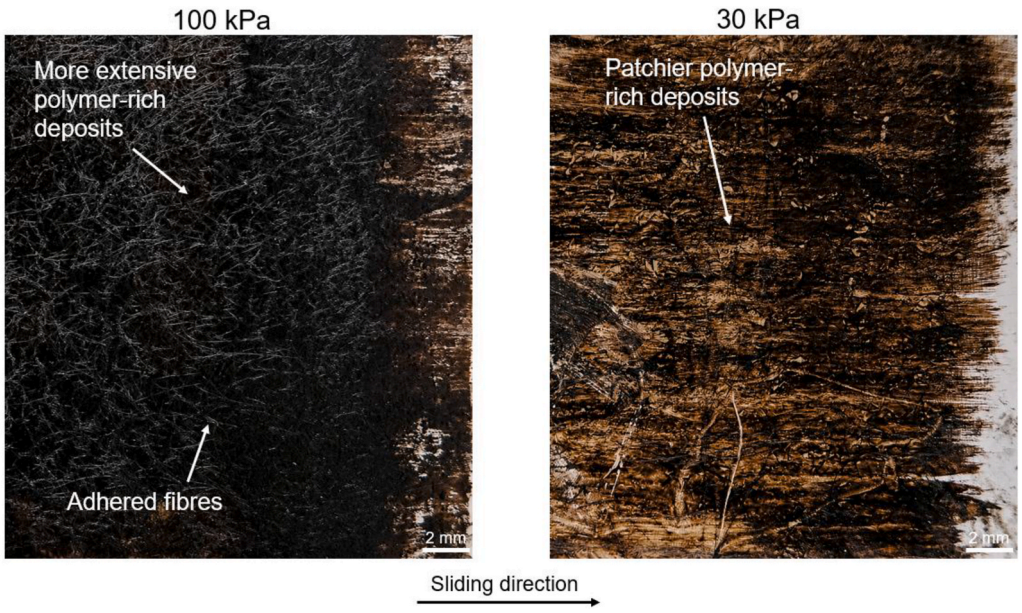


Fig. 12. Post-test aluminium counterfaces from UD-aluminium friction tests at 100 kPa and 30 kPa (left and right, respectively), with T_u/T_{Al} = 190/ 330 °C, v = 200 *mm min*$^{-1}$ and the 0°/Al orientation. The sliding direction is indicated. Scale bars: 2 mm.

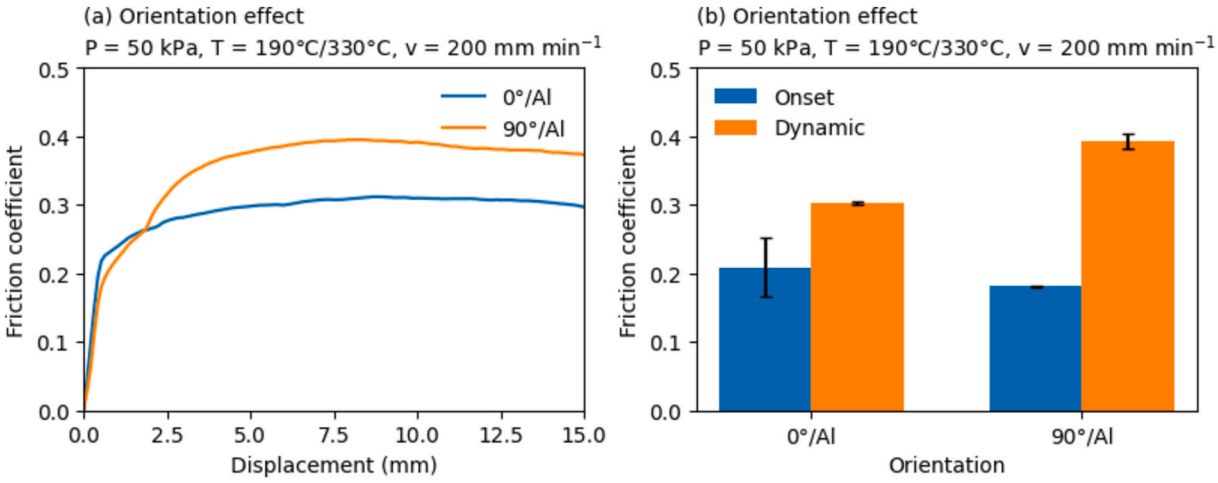


Fig. 13. Influence of orientation on UD-aluminium friction behaviour. (a) μ-displacement curves and (b) corresponding onset and dynamic friction coefficients.

3.4. UD-steel

UD-steel friction was characterised under non-isothermal conditions with independently controlled normal pressure, temperature and slip-rate. In this configuration, the steel counterface was maintained at room temperature, while the UD ply was heated to the target temperature within the solid-state range ($T_u < T_m$). This configuration provides a representative solid-cold metal interface under non-isothermal conditions.

The pressure dependence of the UD-steel interface is shown in Fig. 14 (a) and (d). Increasing the normal pressure reduces both μ_s and μ_k. Higher pressure can promote more uniform contact between the UD surface and the steel counterface and redistribute local contact stresses, which may contribute to the observed reduction in friction coefficient.

The temperature and slip-rate dependence of the UD-steel interface is shown in Fig. 14(b, e) and (c, f). Changing T_u between 180 °C and 200 °C produces negligible variations in μ_s and μ_k. The UD ply was heated below the melting point before contact ($T_u < T_m$), while the steel counterface was at room temperature. The limited temperature and slip-rate effects are consistent with predominantly solid-solid boundary friction in this configuration, rather than a dominant melt-film contribution.

Across all investigated interfaces, increasing normal pressure consistently reduced the friction coefficient, although the associated contact mechanisms differed between interfaces. In contrast, the effects of temperature and slip-rate varied across the investigated interfaces and thermal conditions. Temperature dependence was most evident in the fully molten woven–woven and initially solid–melt UD–woven cases, consistent with changes in melt flow, surface mobility and interfacial lubrication. For the metal-ply cases, temperature sensitivity was limited within the tested range, especially for the solid-cold condition. Slip-rate dependence was clear when a molten interfacial polymer layer contributed to sliding, but became limited when the contact remained predominantly solid-solid. Taken together, these trends show that pressure affected all interfaces in a similar way, whereas the effects of temperature and slip-rate differed across interfaces. Table 3 summarises these comparative characteristics and motivates the interface-specific modelling strategy introduced in the following section.

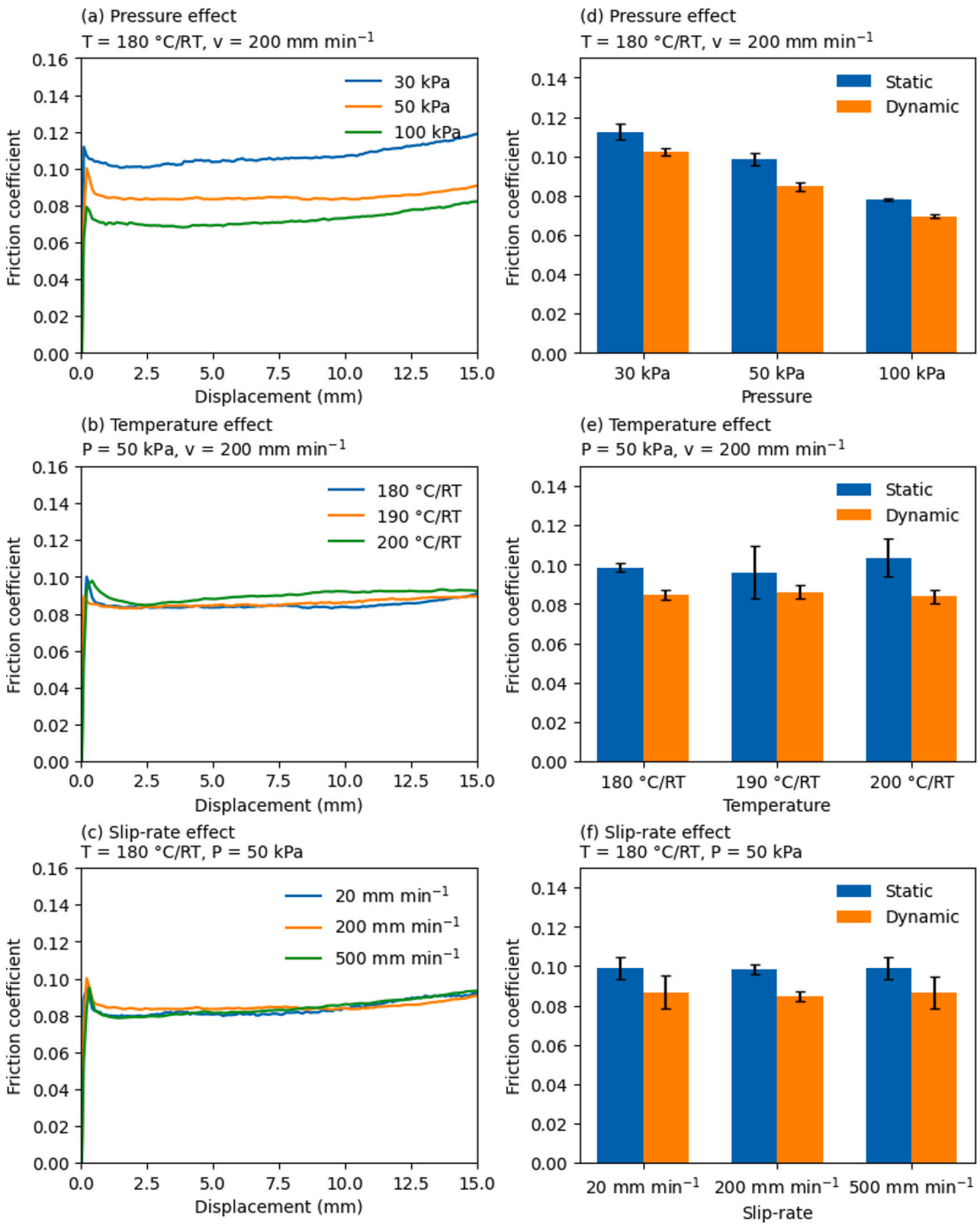


Fig. 14. Influence of normal pressure, temperature and slip-rate on UD-steel friction behaviour. (a-c) μ-displacement curves and (d-f) corresponding static and dynamic friction coefficients.

Table 3
Cross-interface summary of dominant friction characteristics and governing factors.

Interface	Pre-contact thermal state	Normal pressure sensitivity	Temperature sensitivity	Slip-rate sensitivity
Woven-woven	Isothermal, melt-melt	√	√	√
UD-woven	Non-isothermal, solid-melt	√	√	√
UD-aluminium	Non-isothermal, solid-hot metal	√	–	√
UD-steel	Non-isothermal, solid-cold metal	√	–	–

4. Phenomenological friction modelling framework

A common phenomenological modelling framework was adopted for all interfaces investigated in this study. The friction coefficient was expressed as a separable multiplicative function of the governing variables, normalised with respect to a common reference state. Model

forms were guided by diagnostic plots, with initial parameter estimates obtained from linear trends in transformed space, followed by nonlinear least-squares identification using the full dataset. Consistent with the cross-interface experimental synthesis, the woven-woven interface represents the most complete melt-dominated case and therefore serves as the starting point for the formulation of the common framework. The framework is then adapted to the other interfaces according to their dominant mechanisms.

4.1. Woven-woven

A phenomenological model was established to describe woven-woven friction under varying normal pressure, temperature and slip-rate. The dataset comprised three one-dimensional scans around a common reference state defined by $p_{ref} = 50$ kPa, $T_{ref} = 240\,^{\circ}$C, and $v_{ref} = 200$ mm min^{-1}. The friction coefficient was expressed in a separable multiplicative form:

$$\mu_x(T,p,v) = \mu_{0,x} exp\left[-n_x(T - T_{ref})\right]\left(\frac{p}{p_{ref}}\right)^{m_x}\left(\frac{v}{v_{ref}}\right)^{k_x} \quad (4)$$

where x denotes the static or dynamic regime, $\mu_{0,x}$ is the friction coefficient at the reference condition, m_x is the pressure exponent, n_x is the temperature coefficient, and k_x is the slip-rate exponent.

Log-log plots of friction against pressure and slip-rate showed linear behaviour, supporting power-law dependencies, while semi-log plots of friction against temperature showed linear decay, indicating an exponential temperature effect. Initial values of m_x, n_x and k_x were taken from the slopes of the diagnostic plots, while $\mu_{0,x}$ was obtained directly from the measured value at the reference condition. Final parameters were identified by nonlinear least-squares fitting using all available data points.

The fitted exponents follow the physical trends in the melt regime: friction decreases with pressure ($m_x < 0$), decreases with temperature ($n_x > 0$) and increases with slip-rate ($k_x > 0$). The calibrated parameters for the static and dynamic regimes are listed in Table 4.

Fig. 15 compares the measured and predicted woven-woven friction coefficients under isolated variations in normal pressure, temperature and slip-rate. Overall, the static and dynamic model responses capture the main pressure, temperature and slip-rate trends observed in the experiments.

4.2. UD-woven

Building on the common phenomenological framework established for the woven-woven interface, the UD-woven friction response was modelled to account for the coupled dependence on the pre-contact UD and woven surface temperatures. The observed change in UD-temperature sensitivity around the DSC crystallisation peak, together with the change in woven-temperature sensitivity across the tested melt range, motivated the use of a hinge-type exponential temperature map. This temperature map was combined multiplicatively with power-law pressure and slip-rate terms about a common reference state defined by $p_{ref} = 50$ kPa and $v_{ref} = 200$ mm min^{-1}.

The friction coefficient was therefore expressed as:

$$\mu_x(T_u,T_w,p,v) = \mu_{0,x}\exp\left[A_u^- h(T_c - T_u) + A_u^+ h(T_u - T_c) + A_w^- h(T_{cov} - T_w) + A_w^+ h(T_w - T_{cov})\right]\left(\frac{p}{p_{ref}}\right)^{m_x}\left(\frac{v}{v_{ref}}\right)^{k_x} \quad (5)$$

where x denotes the static or dynamic regime and $h(z) = \max(z, 0)$ is the positive-part function, so that only the term on the active side of each breakpoint contributes. The baseline coefficient $\mu_{0,x}$ is defined at $T_u = T_c$, $T_w = T_{cov}$, $p = p_{ref}$ and $v = v_{ref}$. T_c is the UD-temperature breakpoint associated with the DSC crystallisation peak, whereas T_{cov} is the woven-temperature breakpoint used to describe the observed change in temperature sensitivity. The parameters A_u^- and A_u^+ describe the temperature sensitivity below and above T_c, respectively, whereas A_w^- and A_w^+ describe the sensitivity below and above T_{cov}. The parameters m_x and k_x are the pressure and slip-rate exponents.

The use of separate coefficients on either side of each breakpoint allows the model to describe the different temperature sensitivities observed within the sampled range. At fixed T_w, the friction response shows limited sensitivity at lower T_u and a stronger decrease at higher T_u, with the change occurring around the DSC-informed breakpoint T_c. At fixed T_u, friction decreases more strongly as T_w approaches T_{cov}, while the temperature sensitivity becomes weaker at higher T_w. These changes in sensitivity are consistent with the coupled effects of UD surface mobility and woven-matrix flow discussed in Section 3.2.

The UD-temperature breakpoint T_c was fixed at 189 °C with reference to the DSC crystallisation peak and the observed change in T_u sensitivity discussed in Section 3.2. The woven-temperature breakpoint T_{cov} was fitted within the 230–240 °C range based on the change in T_w sensitivity observed experimentally. All remaining parameters were identified using weighted nonlinear least-squares fitting over the full pressure, temperature and slip-rate dataset, with the temperature coefficients shared between the static and dynamic friction descriptions. The calibrated parameters are listed in Table 5.

Fig. 16 compares the measured and predicted friction coefficients for the UD-woven interface under isolated variations of normal pressure, slip-rate and the two pre-contact temperature variables T_u and T_w. Friction decreases with increasing pressure and shows a mild positive dependence on slip-rate, as shown in Fig. 16(a) and (b). At fixed T_w, the response shows limited sensitivity at lower T_u and a stronger decrease at higher T_u, with the change occurring around T_c (Fig. 16(c)). At fixed T_u, the larger reduction in friction occurs as T_w approaches T_{cov}, while the temperature sensitivity becomes weaker at higher T_w (Fig. 16(d–f)). The static and dynamic model responses capture the observed changes in parameter sensitivity across the tested conditions.

4.3. UD-aluminium

For the UD-aluminium interface, the common phenomenological framework was simplified due to the absence of a measurable temperature effect within the identification window. The friction response was therefore described as a function of normal pressure, slip-rate, and fibre orientation about a common reference state defined by $p_{ref} = 50$ kPa and $v_{ref} = 200$ mm min^{-1}.

The friction coefficient was expressed as:

$$\mu_x(p,v,\varphi) = \mu_{0,x}F_x(\varphi)\left(\frac{p}{p_{ref}}\right)^{m_x}\left(\frac{v}{v_{ref}}\right)^{k_x} \quad (6)$$

where x denotes the onset or dynamic regime, $\mu_{0,x}$ is the friction coefficient at the reference condition for the 0°/Al configuration, $F_x(\varphi)$ is the orientation factor, m_x and k_x are the pressure and slip-rate exponents, respectively.

The orientation factor $F_x(\varphi)$ was defined relative to the 0°/Al baseline. Accordingly, $F_x = 1$ for the 0°/Al configuration, whereas for the

Table 4
Calibrated parameters for woven-woven contact.

Parameter	Notation	Static	Dynamic
Baseline friction coefficient	$\mu_{0,x}$	0.334	0.221
Pressure exponent	m_x	−1.1725	−0.939
Temperature coefficient	n_x	0.027	0.0324
Slip-rate exponent	k_x	1.090	1.094

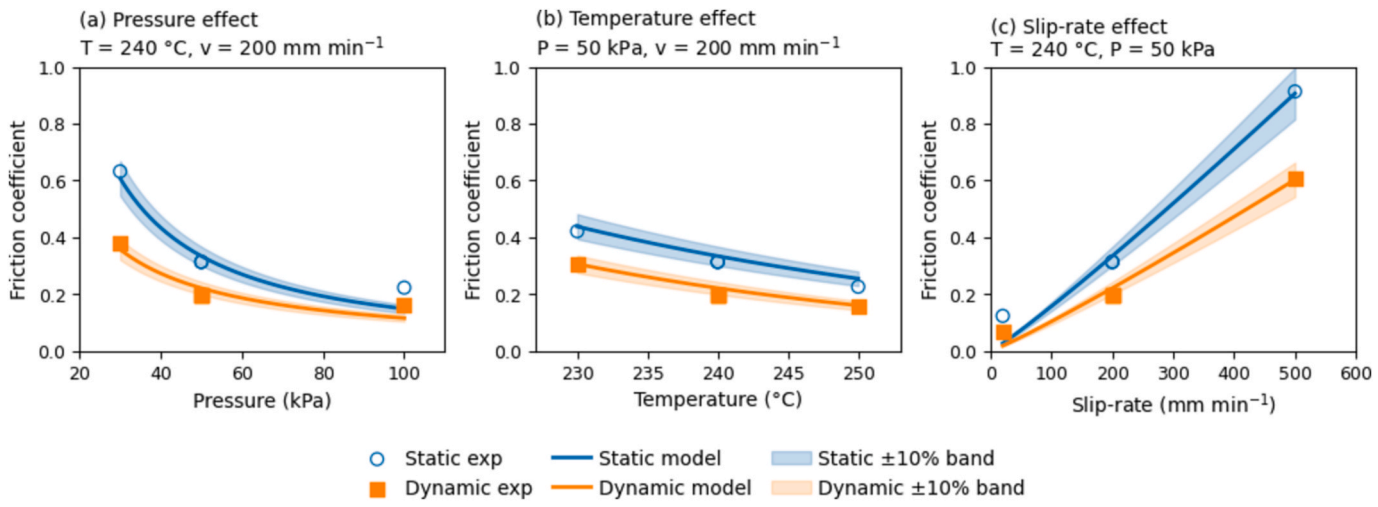


Fig. 15. Comparison between measured and model-predicted woven-woven friction coefficients under (a) normal pressure, (b) temperature and (c) slip-rate variations.

Table 5
Calibrated parameters for UD-woven contact.

Parameter	Notation	Value	Unit
UD temperature breakpoint	T_c	189	$^\circ C$
Woven temperature breakpoint	T_{cov}	235	$^\circ C$
UD temperature coefficient above T_c	A_u^+	−0.030	$^\circ C^{-1}$
UD temperature coefficient below T_c	A_u^-	−0.002	$^\circ C^{-1}$
Woven temperature coefficient above T_{cov}	A_w^+	0.005	$^\circ C^{-1}$
Woven temperature coefficient below T_{cov}	A_w^-	0.145	$^\circ C^{-1}$
Baseline static friction coefficient	$\mu_{0,s}$	0.155	–
Baseline dynamic friction coefficient	$\mu_{0,d}$	0.133	–
Pressure exponent for static friction	m_s	−0.817	–
Pressure exponent for dynamic friction	m_d	−0.807	–
Slip-rate exponent for static friction	k_s	0.264	–
Slip-rate exponent for dynamic friction	k_d	0.175	–

90°/Al configuration F_x represents the ratio between the friction levels of the 90°/Al and 0°/Al cases at the reference condition. Model parameters were identified using nonlinear least-squares fitting. The fitted exponents follow the observed trends, with friction decreasing with pressure ($m_x < 0$) and increasing with slip-rate ($k_x > 0$). The calibrated parameters for the onset and dynamic regimes are listed in Table 6.

Fig. 17 compares the measured and predicted friction coefficients for the UD-aluminium interface under variations of pressure and slip-rate for the two fibre orientations. For the 0°/Al configuration, friction decreases monotonically with increasing pressure and shows a moderate positive dependence on slip-rate. For the 90°/Al configuration, the dynamic friction level is higher than that of 0°/Al due to the greater tangential resistance associated with transverse fibres. Overall, the onset and dynamic model responses capture the main parameter trends observed in the experiments.

4.4. UD-steel

For the UD-steel interface, temperature and slip-rate showed negligible influence within the identification window and were therefore held at their reference values. The friction response was represented using a pressure-only power-law model about a common reference state defined by $p_{ref} = 50$ kPa, corresponding to a limiting case of the common framework.

The friction coefficient was expressed as:

$$\mu_x(p) = \mu_{0,x}\left(\frac{p}{p_{ref}}\right)^{m_x} \tag{7}$$

where x denotes the static or dynamic regime, $\mu_{0,x}$ is the friction coefficient at the reference condition, and m_x is the pressure exponent. Model parameters were identified by nonlinear least-squares fitting, and the calibrated values are listed in Table 7.

Fig. 18 compares the measured and predicted friction coefficients for the UD-steel interface under varying normal pressure. Both static and dynamic coefficients decrease monotonically with pressure, and the fitted pressure-only model shows close agreement with the experimental data while reproducing the parameter trend across the tested range.

4.5. Model comparison and applicability

Across the four interfaces, the form of the models follows a common multiplicative framework, but the retained terms vary with the governing mechanisms. Woven-woven serves as the baseline fully molten case and retains terms that model the effects of pressure, temperature and slip-rate. The UD-woven model extends this form through two breakpoint-based temperature terms describing the coupled dependence on the pre-contact UD and woven temperatures. The UD-aluminium model retains terms that model the effects of pressure, slip-rate and orientation, whereas the UD-steel model reduces to a pressure-only form. These differences show that the same model framework can be simplified or extended for different interfaces.

The calibrated models should be interpreted as empirical, in-range descriptions of the present datasets. Their applicability is therefore limited to the investigated pressure, temperature and slip-rate ranges, and orientation where relevant. Extension to wider temperature ranges depends on whether the thermal configuration underlying each model is maintained. For woven–woven contact, the existing temperature-dependent form may remain useful at nearby higher temperatures if fully molten contact is maintained; however, it should not be directly extrapolated towards or below the melting range without additional characterisation, because the fully molten contact condition may no longer apply. For UD–woven contact, the present model should not be directly extrapolated to conditions where the UD pre-contact temperature approaches or exceeds the melting range, or where the woven temperature decreases towards or below it, because the initially solid–melt configuration may no longer be maintained. For UD–aluminium, the limited temperature sensitivity was observed only along the paired conditions of 180/320, 190/330 and 200/340 °C, so other temperature combinations may require explicit temperature-dependent terms. For UD–steel, the pressure-only form applies to the tested configuration of a sub-melting UD ply against a room-temperature steel counterface; a heated steel counterface or a UD ply approaching melting would require

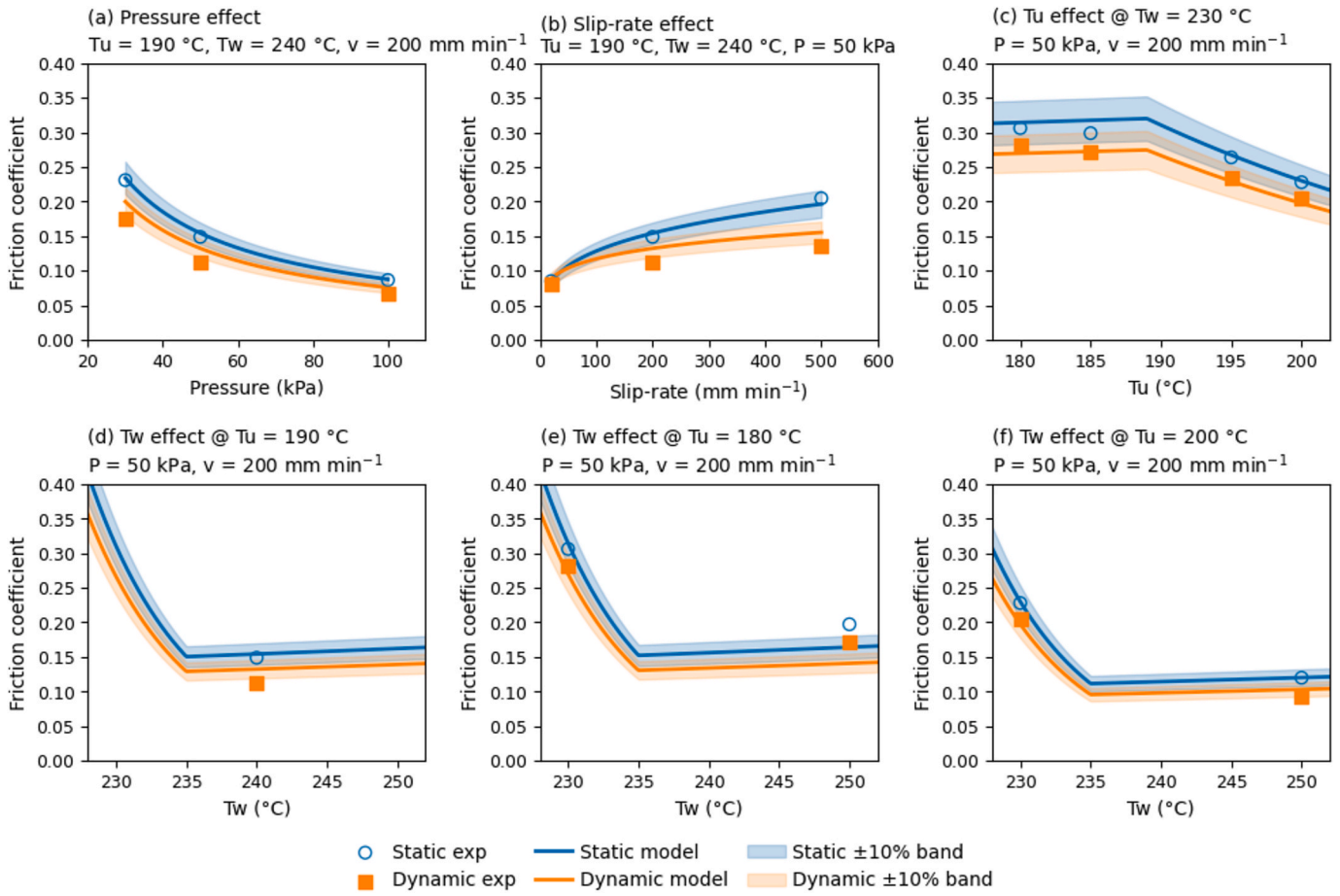


Fig. 16. Comparison between measured and model-predicted friction coefficients for the UD-woven interface under isolated variations of (a) normal pressure, (b) slip-rate, (c) UD temperature at fixed T_w and (d-f) woven temperature at three fixed T_u.

Table 6
Calibrated parameters for UD-aluminium contact.

Parameter	Notation	Onset	Dynamic
Baseline friction coefficient at 0°/Al	$\mu_{0,x}$	0.209	0.303
Orientation factor at 90°/Al	F_x	0.867	1.298
Pressure exponent	m_x	−1.625	−1.237
Slip-rate exponent	k_x	0.522	0.554

reassessment of the model form.

The current fits are intended for interpolation within the sampled thermal paths and have not been validated for wider-temperature prediction. At MPa-level pressures, stronger polymer squeeze-out and increased fibre–tool contact may alter the governing friction behaviour. Extension beyond the tested pressure and temperature conditions would therefore require additional experimental characterisation and recalibration, with the model form reassessed where the initial thermal/contact state or governing friction mechanism changes.

5. Conclusions

Interfacial friction of four CF/PA6 interfaces was characterised under isothermal and non-isothermal conditions using a newly developed pull-through rig. Phenomenological models were established to describe the dominant parameter effects for each interface. The main conclusions are as follows.

(1) A pull-through rig with integrated thermal and pressure control was developed to enable systematic measurement of interfacial friction under independently controlled normal pressure, temperature, slip-rate and fibre orientation. The methodology was applied to both ply-ply and metal-ply interfaces under isothermal and non-isothermal conditions.

(2) Within the tested 30–100 kPa range, increasing normal pressure reduced the friction coefficient across all four interfaces. This reduction was observed despite differences in interface type and pre-contact thermal state.

(3) The results support interface-dependent friction mechanisms. Woven-woven friction was consistent with a substantial viscous-shear contribution within the melt film. UD-woven friction depended on both pre-contact temperatures, with the friction trends and post-test morphology supporting roles for UD surface mobility, melt coverage and polymer redistribution. UD-aluminium friction was consistent with polymer-mediated shear and local fibre-metal contact and showed limited temperature sensitivity within the tested range. The UD-steel response was

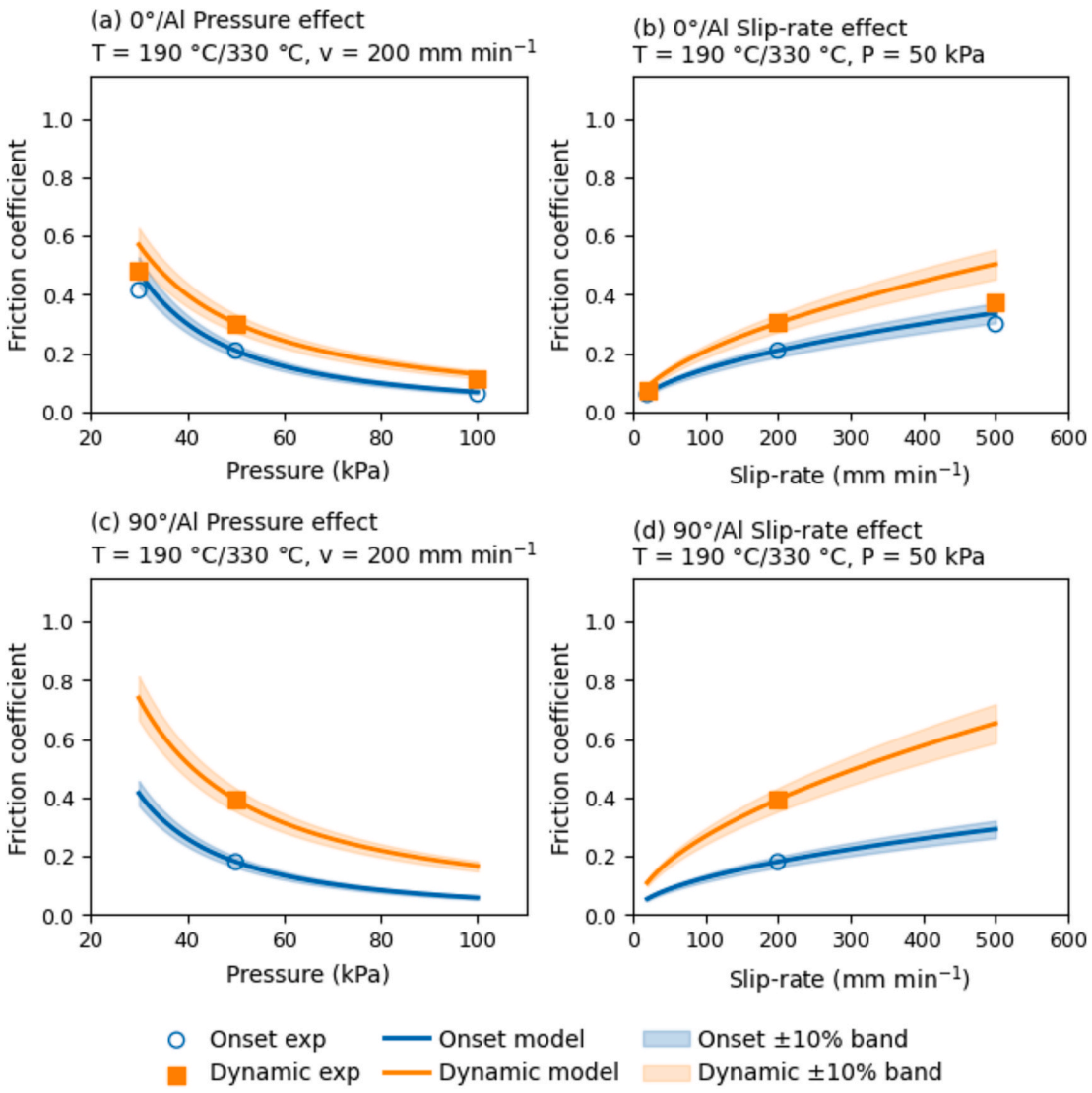


Fig. 17. Comparison between measured and model-predicted UD-aluminium friction coefficients under (a, b) the 0°/Al fibre orientation and (c, d) the 90°/Al orientation.

Table 7
Calibrated parameters for UD-steel contact.

Parameter	Notation	Static	Dynamic
Baseline friction coefficient	$\mu_{0,x}$	0.097	0.086
Pressure exponent	m_x	−0.305	−0.320

consistent with predominantly solid-solid boundary friction and exhibited limited temperature and slip-rate dependence.

(4) A common phenomenological modelling framework was established for all four interfaces. The woven-woven model retained pressure, temperature and slip-rate as the baseline fully molten case. The UD-woven model extended this framework through coupled breakpoint-based pre-contact-temperature terms. The UD-aluminium model retained pressure, slip-rate and orientation, whereas the UD-steel model retained only pressure. The resulting models reproduced the measured trends and provided compact empirical descriptions of the investigated interface responses.

Beyond the CF/PA6 system and conditions studied here, the proposed experimental and modelling framework provides a basis for

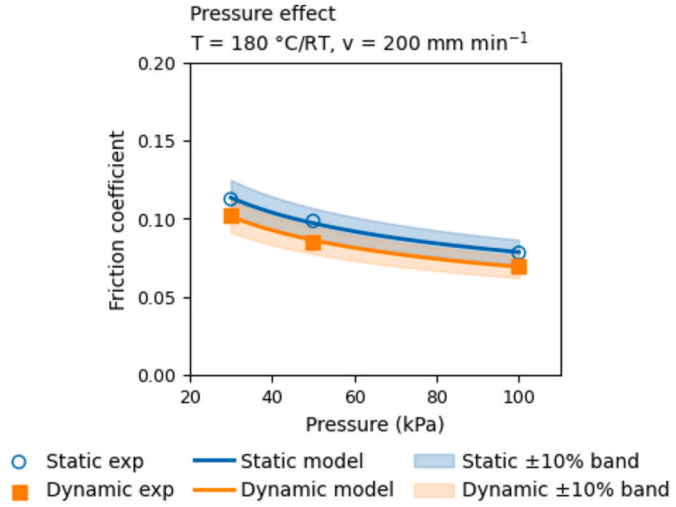


Fig. 18. Comparison between measured and model-predicted UD-steel friction coefficients under isolated variations of normal pressure.

characterisation over wider temperature ranges and for other thermoplastic composite and fibre-metal laminate systems. Such extensions require material- and range-specific characterisation, calibration and validation, with revision of the model form where the governing friction mechanism changes.

CRediT authorship contribution statement

Chunyi Gao: Writing – original draft, Visualization, Validation, Methodology, Investigation, Formal analysis, Data curation, Conceptualization. **Bamber Blackman:** Writing – review & editing, Supervision, Resources, Methodology, Formal analysis. **Zerong Ding:** Writing – review & editing, Methodology, Conceptualization. **Nan Li:** Writing – review & editing, Supervision, Project administration, Methodology, Investigation, Funding acquisition, Formal analysis, Conceptualization.

Declaration of competing interest

The authors declare that they have no known competing financial interests or personal relationships that could have appeared to influence the work reported in this paper.

Acknowledgements

Chunyi Gao acknowledges the PhD Scholarship from Imperial College London. In addition, the authors appreciate the support from Mr Suresh Viswanathan on the experiments. For the purpose of open access, the author has applied a Creative Commons Attribution (CC BY) license to any Author Accepted Manuscript version arising.

Appendix A. Surface-temperature calibration and contact-dwell measurement

Figure A1(a) presents the representative pre-contact surface-temperature calibration histories at target temperatures of 180, 190 and 200 °C. A small periodic temperature oscillation remained during steady heating due to the PID-controlled heater duty cycle. At the 200 °C condition, the stabilised half-amplitude was approximately 0.51 °C.

A representative UD–woven contact-dwell measurement was performed with target pre-contact UD and woven surface temperatures of 200 °C and 250 °C, respectively, at 50 kPa (Figure A1(b)). The measurement was performed without relative sliding because the surface-attached thermocouples and fixing tape would disturb the local contact and be displaced during motion. Temperature histories were recorded at 0.2 s intervals. Over the first 60 s after contact, the mean thermocouple readings were 221.34 °C on the UD side and 222.36 °C on the woven side.

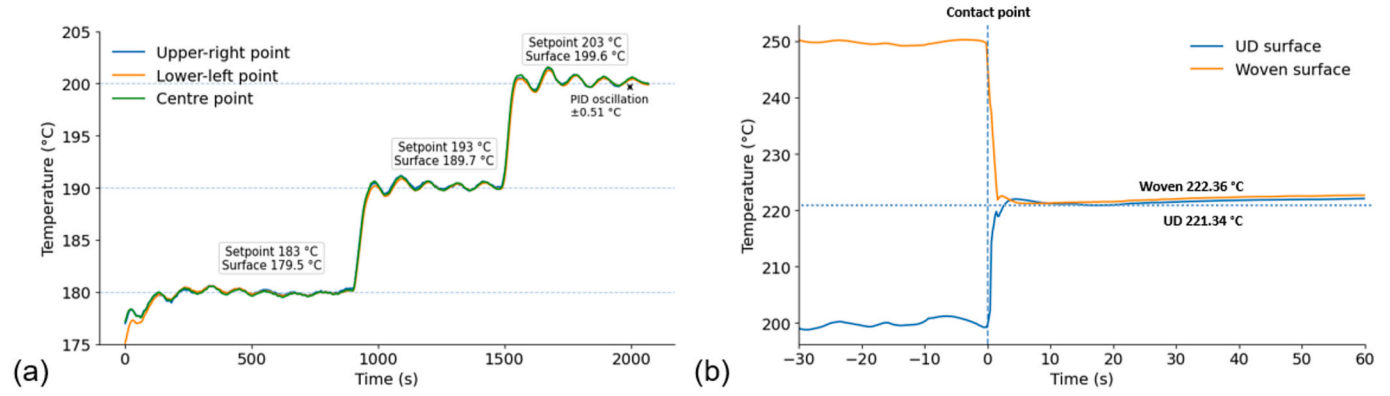


Fig. A1. Surface-temperature calibration and contact-dwell measurement. (a) Representative pre-contact temperature histories measured at three surface locations at target temperatures of 180, 190 and 200 °C. (b) Temperature histories measured during a representative UD–woven contact-dwell test without relative sliding, with target pre-contact UD and woven surface temperatures of 200 °C and 250 °C, respectively, at 50 kPa. The annotations in (b) show mean thermocouple readings over the first 60 s after contact.

Appendix B. Definition sensitivity of the interface-specific early-stage extraction

Figure B1 compares the common fixed-displacement coefficient, $\mu_{0.5} = \mu\,(0.50\ mm)$, with the primary interface-specific early-stage values for all 42 test conditions. The absolute percentage differences relative to the primary values were first averaged within each interface and then averaged across the four interfaces with equal weighting. The interface-balanced mean absolute percentage difference was 9.4%. The numerical differences reflect the different shapes of the early-stage responses. For woven–woven and UD–woven conditions with pronounced peaks beyond 0.50 mm, the fixed-displacement value samples the rising response before the peak. For UD–steel, the early local maximum occurs before 0.50 mm, so the fixed-displacement value samples the subsequent response. In contrast, the difference is small for UD–aluminium because its onset descriptor is already taken at the first sampled point beyond 0.50 mm. All 13 parameter groups retained the same direction of change between their first and last conditions, and the complete within-group ranking was preserved in 12 of 13 groups. The only change in ranking occurred in the closely clustered UD–steel temperature series, for which neither extraction method showed a clear monotonic temperature trend.

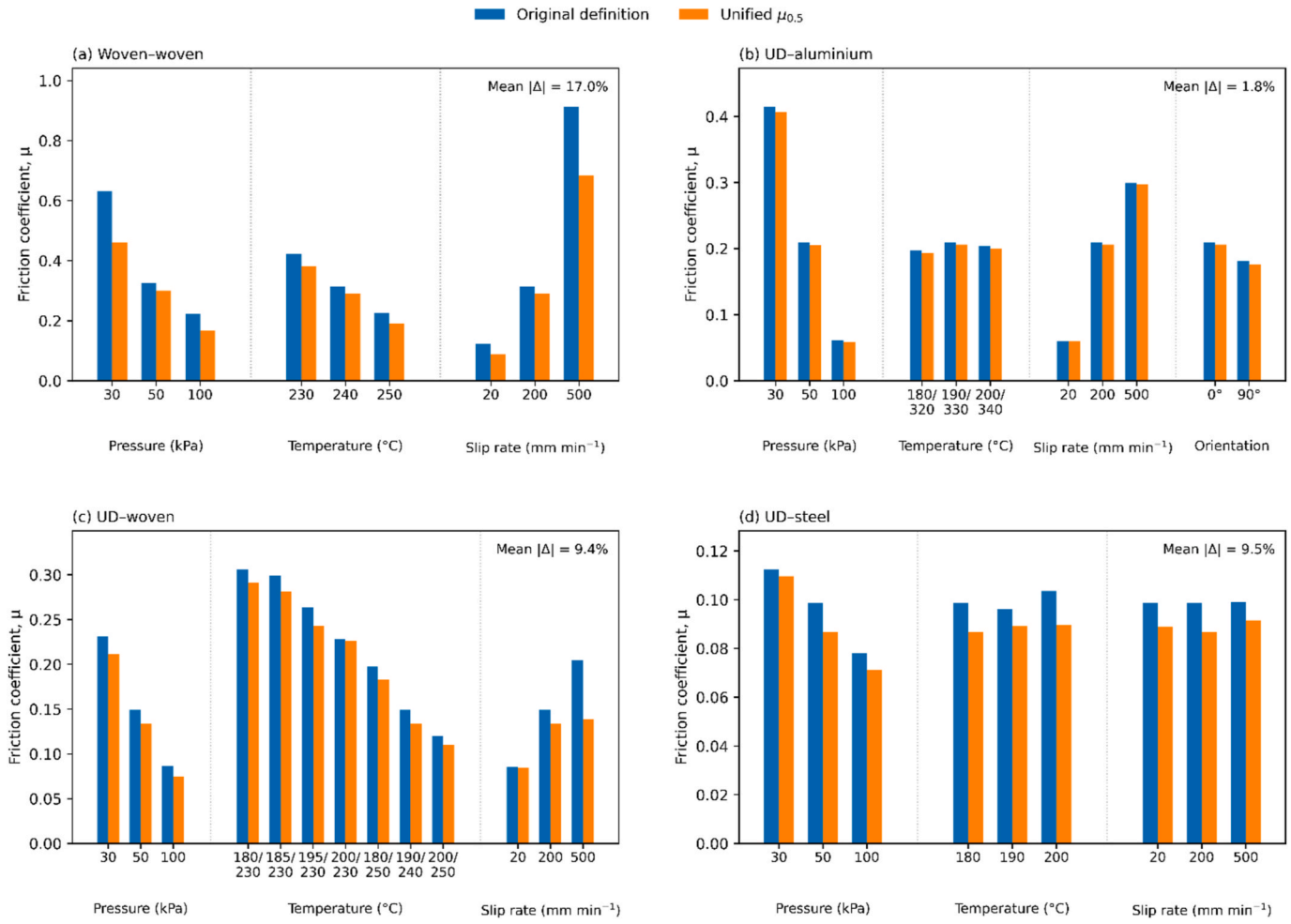


Fig. B1. Comparison of the original interface-specific early-stage values and the common fixed-displacement metric, $\mu_{0.5} = \mu\,(0.50\,mm)$, for all 42 test conditions. The mean |Δ| reported in each panel is the mean absolute percentage difference for the corresponding interface.

Appendix C. Repeatability of the friction response

Figure C1 presents triplicate μ-displacement curves for representative parameter scans of all four interface types. Pressure-dependent repeatability is shown for woven–woven, UD–woven, UD–aluminium and UD–steel contact, together with an additional woven–woven slip-rate scan covering the pronounced high-rate peak response. The individual curves are presented without averaging or numerical smoothing.

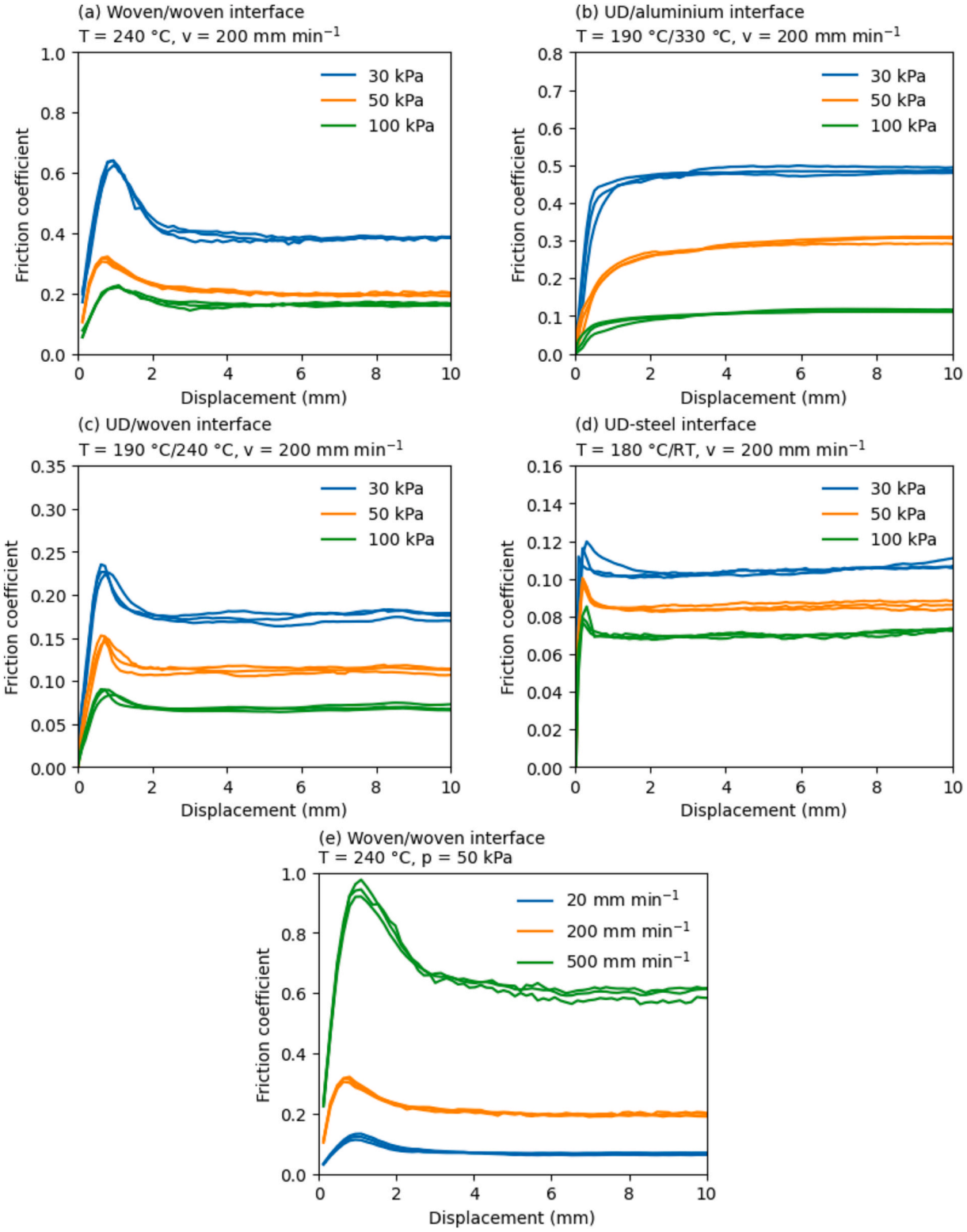


Fig. C1. Triplicate μ-displacement curves for representative pressure and slip-rate scans: (a) woven–woven pressure, (b) UD–aluminium pressure, (c) UD–woven pressure, (d) UD–steel pressure and (e) woven–woven slip-rate. The individual curves are presented without averaging or numerical smoothing.

Data availability

Data will be made available on request.

References

[1] Lee J-M, Kim B-M, Lee C-J, Ko D-C. A characterisation of tool-ply friction behaviors in thermoplastic composite. Procedia Eng 2017;207:90–4. https://doi.org/10.1016/j.proeng.2017.10.743.

[2] Brooks R. Forming technology for thermoplastic composites. In: Long AC, editor. Composites forming technologies. Cambridge, *UK*: Woodhead Publishing; 2007. p. 256–76. https://doi.org/10.1533/9781845692537.256.

[3] Brooks RA, et al. A review on stamp forming of continuous fibre-reinforced thermoplastics. Int J Lightweight Mater Manuf 2022;5(3):411–30. https://doi.org/10.1016/j.ijlmm.2022.05.001.

[4] Joustra J, Brans K, Fernandez Villegas I, Sinke J, Teuwen J. Reverse forming thermoplastic composites: design and process development. Composites Part C: Open Access 2025;16:100550. https://doi.org/10.1016/j.jcomc.2024.100550.

[5] Sachs U. Friction and bending in thermoplastic composites forming processes. Enschede, The Netherlands: University of Twente; 2014. https://doi.org/10.3990/1.9789462594838. Ph.D. thesis.

[6] Deng T, et al. A hybrid lamination model for simulation of woven fabric reinforced thermoplastic composites solid-state thermo-stamping. Mater Des 2021;200:109419. https://doi.org/10.1016/j.matdes.2020.109419.

[7] Wang H, Ding Z, Chen X, Liu H, Li N. Experimental characterisation and constitutive modelling of the intra-ply tensile and shear properties of unidirectional fibre reinforced thermoplastics (UD FRTPs) under solid-state stamp forming conditions. Compos Appl Sci Manuf 2024;179:108034. https://doi.org/10.1016/j.compositesa.2024.108034.

[8] Dörr D. Simulation of the thermoforming process of UD fiber-reinforced thermoplastic tape laminates. Karlsruhe, Germany: Karlsruhe Institute of Technology (KIT); 2021. https://doi.org/10.5445/KSP/1000099858. Ph.D. dissertation.

[9] Zhang B, Kim BC. Experimental characterisation of large in-plane shear behaviour of unidirectional carbon fibre/epoxy prepreg tapes for continuous tow shearing (CTS) process. Compos Appl Sci Manuf 2022;162:107168. https://doi.org/10.1016/j.compositesa.2022.107168.

[10] Pasco C, Khan M, Gupta J, Kendall K. Experimental investigation on interply friction properties of thermoset prepreg systems. J Compos Mater 2019;53(2):227–43. https://doi.org/10.1177/0021998318781706.

[11] Laresser D. Investigation of the forming behavior of a thermoplastic unidirectional tape laminate: forming experiment, modeling. Master's thesis. Linz, Austria: Johannes Kepler University Linz; 2020.

[12] Bortoleto EM, et al. Experimental and numerical analysis of dry contact in the pin on disc test. Wear 2013;301(1–2):19–26. https://doi.org/10.1016/j.wear.2012.12.005.

[13] Campos D, Maimí P, Martín A. Characterization of interlaminar friction during the forming processes of high-performance thermoplastic composites. J Compos Sci 2024;8(2):38 [Online]. Available: https://www.mdpi.com/2504-477X/8/2/38.

[14] Das A, Choong GYH, Dillard DA, De Focatiis DSA, Bortner MJ. Characterizing friction for fiber reinforced composites manufacturing: method development and effect of process parameters. Compos B Eng 2022;236:109777. https://doi.org/10.1016/j.compositesb.2022.109777.

[15] Kapshammer A, Laresser D, Miron MC, Baudach F, Major Z. Characterization and modeling of Ply/Tool and Ply/Ply slippage phenomena of unidirectional polycarbonate CF tapes. Polymers 2023;15(17):3520 [Online]. Available: https://www.mdpi.com/2073-4360/15/17/3520.

[16] Nur TJ, Ryan CA, Bajwa DS, Cairns DS, Ridgard C, Amendola R. Characterization of frictional behavior of fiber reinforced composites during forming: a review. Compos Appl Sci Manuf 2025;193:108852. https://doi.org/10.1016/j.compositesa.2025.108852.

[17] Sachs U, et al. Characterization of the dynamic friction of woven fabrics: experimental methods and benchmark results. Compos Appl Sci Manuf 2014;67:289–98. https://doi.org/10.1016/j.compositesa.2014.08.026.

[18] Zheng K, Politis DJ, Wang L, Lin J. A review on forming techniques for manufacturing lightweight complex—shaped aluminium panel components. Int J Lightweight Mater Manuf 2018;1(2):55–80. https://doi.org/10.1016/j.ijlmm.2018.03.006.

[19] Street GE, Johnson MS. The intra-ply shear behaviour of non-isothermal thermoplastic composite laminates. J Compos Sci 2023;7(10):432. https://doi.org/10.3390/jcs7100432.

[20] Lagarinhos J, Magalhães da Silva S, Oliveira JM. Non-Isothermal crystallization kinetics of polyamide 6/Graphene nanoplatelets nanocomposites obtained via in situ polymerization: effect of nanofiller size. Polymers 2023;15(20):4109. https://doi.org/10.3390/polym15204109.

[21] Nasr A, Svoboda P. Influence of fusion temperature on nonisothermal crystallization kinetics of polyamide 6. Polymers 2023;15(8):1952. https://doi.org/10.3390/polym15081952.

[22] Liu Z, Simonetto E, Ghiotti A, Bruschi S. Modelling of fiber metal laminates thermoforming using superimposed membrane-shell elements. Int J Mech Sci 2025;302:110518. https://doi.org/10.1016/j.ijmecsci.2025.110518.

[23] Lin Q, Christian WJR, Guan Z. Quantitative validation of finite element models of fibre metal laminate thermo-forming. J Sandw Struct Mater 2025;27(5):1063–89. https://doi.org/10.1177/10996362251327965.

[24] Zhang W, Wang L, Peng X. Ply-ply friction behavior between unidirectional thermoplastic prepreg plies during thermoforming: characterization and modeling. Mater Des 2024;247:113426. https://doi.org/10.1016/j.matdes.2024.113426.

[25] ten Thije RHW, Akkerman R, van der Meer L, Ubbink MP. Tool-ply friction in thermoplastic composite forming. Int J Material Form 2008;1(suppl. 1):953–6. https://doi.org/10.1007/s12289-008-0215-9.

[26] Liu Z, Simonetto E, Ghiotti A, Bruschi S. Inter-ply friction behaviour in the temperature assisted forming of magnesium/glass fibre reinforced thermoplastic polymer laminates. Compos Appl Sci Manuf 2023;173:107635. https://doi.org/10.1016/j.compositesa.2023.107635.

[27] Zhang W, Zhou H, Huang B, Zhou H, Peng X. Characterization of tool-ply friction behavior for treated jute/PLA biocomposite prepregs in thermoforming. Compos Appl Sci Manuf 2024;177:107875. https://doi.org/10.1016/j.compositesa.2023.107875.

[28] Pierik ER, Grouve WJB, Wijskamp S, Akkerman R. Prediction of the peak and steady-state ply–ply friction response for UD C/PAEK tapes. Compos Appl Sci Manuf 2022;163:107185. https://doi.org/10.1016/j.compositesa.2022.107185.

[29] Dörr D, Faisst M, Joppich T, Poppe C, Henning F, Kärger L. Modelling approach for anisotropic inter-ply slippage in finite element forming simulation of thermoplastic UD-tapes. AIP Conf Proc 2018;1960(1):020005. https://doi.org/10.1063/1.5034806.

[30] Dörr D, et al. A benchmark study of finite element codes for forming simulation of thermoplastic UD-Tapes. Proced CIRP 2017;66:101–6. https://doi.org/10.1016/j.procir.2017.03.223.

[31] Lang M. Charakterisierung der Reibeigenschaften von PA6- und PPS-UD-Tape. In: Master's thesis, Institute of Applied Materials. Karlsruhe, Germany: Karlsruhe Institute of Technology (KIT); 2015.

[32] Liu Y, Wu Q, Duan S, Zhao G, Xiong K. Investigation of tool-part interaction in thermoplastic composite press consolidation using embedded fiber Bragg grating. Compos Appl Sci Manuf 2026;206:109778. https://doi.org/10.1016/j.compositesa.2026.109778.

[33] Liu S, Sinke J, Dransfeld C. An inter-ply friction model for thermoset based fibre metal laminate in a hot-pressing process. Compos B Eng 2021;227:109400. https://doi.org/10.1016/j.compositesb.2021.109400.

[34] Lessard H, Lebrun G, Benkaddour A, Pham X-T. Influence of process parameters on the thermostamping of a [0/90]12 carbon/polyether ether ketone laminate. Compos Appl Sci Manuf 2015;70:59–68. https://doi.org/10.1016/j.compositesa.2014.12.009.

[35] Fetfatsidis KA, Jauffrès D, Sherwood JA, Chen J. Characterization of the tool/fabric and fabric/fabric friction for woven-fabric composites during the thermostamping process. Int J Material Form 2013;6(2):209–21. https://doi.org/10.1007/s12289-011-1072-5.

[36] Clifford MJ, Long AC, de Luca P. Forming of engineered prepregs and reinforced thermoplastics. In: *Second global symposium on innovations in materials processing and manufacturing: sheet materials*, New Orleans, LA, USA; 2001. p. 303–16.

[37] Gorczyca JL, Sherwood JA, Liu L, Chen J. Modeling of friction and shear in thermostamping of composites—Part I. J Compos Mater 2004;38(21):1911–29. https://doi.org/10.1177/0021998304048416.

[38] Wang L, Wang J, Liu M, Peng X. Development and verification of a finite element model for double diaphragm preforming of unidirectional carbon fiber prepreg. Compos Appl Sci Manuf 2020;135:105924. https://doi.org/10.1016/j.compositesa.2020.105924.

[39] Zhang W, Liao H, Wang L, Peng X. A prepreg-tool slipping model for unidirectional CF/PPS prepreg during hot-stamping process. Compos Appl Sci Manuf 2025;199:109239. https://doi.org/10.1016/j.compositesa.2025.109239.

[40] Toray Advanced Composites. Toray Cetex® TC910 PA6 product data sheet [Online]. Available: Toray Advanced Composites website (accessed 10 February 2026).

[41] Envalior. Tepex® dynalite 202-C200(x)/45%: Material data sheet [Online]. Available: Envalior Plastics Finder (accessed 12 September 2026).

[42] Winhard J, Nestler D, Kroll L. Effects of process parameters in thermoforming of unidirectional fibre-reinforced thermoplastics. Polymers 2024;16(2):221. https://doi.org/10.3390/polym16020221.

[43] Limaye M, et al. Thermoforming process effects on structural performance of carbon fiber reinforced thermoplastic composite parts through a manufacturing to response pathway. Compos B Eng 2022;235:109728. https://doi.org/10.1016/j.compositesb.2022.109728.

[44] Hutchings IM, Shipway P. Tribology: friction and wear of engineering materials. second ed. Oxford: Butterworth-Heinemann; 2017.

[45] Simaafrookhteh S, Carlesso P, Callens MG, Dorigato A, Lomov SV, Ivens J. Temperature-dependent effective viscosity of unidirectional CF/PA6 thermoplastic prepreg tapes during consolidation. Proceedings of the 21st European Conference on Composite Materials (ECCM21), Nantes, France 2-5 July 2024;8:1285–92.

[46] Robinson JW, Zhou Y, Bhattacharya P, Erck R, Qu J, Bays JT, Cosimbescu L. Probing the molecular design of hyper-branched aryl polyesters towards lubricant applications. Sci Rep 2016;6:18624. https://doi.org/10.1038/srep18624.